Contract No:

This document was prepared in conjunction with work accomplished under Contract No. 89303321CEM000080 with the U.S. Department of Energy (DOE) Office of Environmental Management (EM).

Disclaimer:

H-Canyon Dissolver Offgas Monitoring Using Raman Spectroscopy

R.J. Lascola

P.E. O'Rourke

D.M. Immel

E. Larson

January 2022

SRNL-STI-2021-00451, Revision 0

DISCLAIMER

Printed in the United States of America

Prepared for
U.S. Department of Energy

SRNL-STI-2021-00451
Revision 0

Keywords: *Instrumentation, online monitoring, process control*

Retention: *Varies*

H-Canyon Dissolver Offgas Monitoring Using Raman Spectroscopy

R.J. Lascola
P.E. O'Rourke
D.M. Immel
E. Larson

January 2022

Savannah River National Laboratory is operated by Battelle Savannah River Alliance for the U.S. Department of Energy under Contract No. 89303321CEM000080.

REVIEWS AND APPROVALS

AUTHORS:

_____
R.J. Lascola, Sensing and Metrology Division Date

_____
P.E. O'Rourke, Sensing and Metrology Division Date

TECHNICAL REVIEW:

_____
W.E. Daniel, Jr., Actinide & Separations Science, Reviewed per E7 2.60 Date

APPROVAL:

_____
M.L. Whitehead, Manager Date
Sensing and Metrology Division

_____
M.M. Reigel, Manager Date
Materials Technology Division

_____
D.T. Herman, Nuclear Materials Systems Division, SRNL ABD Program Manager Date

_____
A.M. Hudlow, Manager Date
Materials Disposition Engineering

ACKNOWLEDGEMENTS

The successful implementation of the Raman analyzer would not have been possible without the collaboration of members of the SRNL Nonproliferation & Safeguards Division (R. Jeffcoat, J. DeGange, J. Gue, J. Mannion, and D. Padgett), who allowed us to install our instrument in their analytical trailer. They also helped coordinate our activities with those of H-Canyon Operations and Radiological Protection. Many fruitful discussions with members of H-Canyon Engineering (W. Clifton, T. Smith, J. Therrell, J. Fitzpatrick, N. Smith, and S. Brown) helped us better understand how the process was operated, the challenges and concerns associated with making the operation more efficient, and how the analyzer could be most useful in achieving that goal. Insight into the chemistry of the process was provided by members of SRNL's Actinide & Separation Science (T. Rudisill, W. Daniel) and Chemical Processing (K. Taylor-Pashow) Divisions. Also, the first versions of the analyzer were developed to support lab-scale experiments led by these groups. Finally, the enthusiastic support of SRNL and H-Canyon management and their belief that the Raman analyzer could contribute to the goal of improved dissolver process operations drove the project forward and allowed us the chance to test and expand upon our ideas.

EXECUTIVE SUMMARY

This report describes the development and in facility demonstration of a Raman spectrometer to monitor known aluminum offgas components generated during the dissolution of Spent Nuclear Fuel at the Savannah River Site H-Canyon facility. The presence of these gases is an indicator that material is actively being dissolved. This process monitoring technique, which measures the offgas in real time, has the potential to improve the efficiency of facility operations. If the dissolution time is too short, time is wasted due to extended dissolution periods with additional probing of the dissolver pot to confirm that fragment levels are below the thresholds for continuing to the next charge or moving the dissolvent to a receiving tank. If the dissolution time is too long, time and energy are wasted.

The Raman spectrometer was deployed inside an air-conditioned trailer, owned by SRNL, located adjacent to H-Canyon that is tied into the offgas line. The trailer can be configured to monitor either the 6.1D or 6.4D dissolver offgas stream. The instrument is capable of simultaneously measuring multiple aluminum offgas components, including N_2O, NO, NO_2, H_2, H_2O, N_2, and O_2. The instrument control and data interpretation routine, written by SRNL, includes a provision for automatically correcting recorded spectra for wavelength drift caused by temperature changes in the trailer. The software automatically applies calibration models to extract gas concentrations (as percentages of the total stream) from the spectra. Two configurations of the instrument were tested, using either a 532 nm or a 640 nm laser to generate the Raman signal.

The monitor was tested on 15 dissolutions. Seven dissolutions/charges were associated with Material Test Reactor (MTR) fuel (three batches) being dissolved in dissolver 6.1D. Of these dissolutions/charges, six were associated with the (3,4,5) bundle charging scheme (MTR Batches 22 and 24) and one was associated with the (6,6) charging scheme (MTR Batch 26, first charge only). Eight dissolutions/charges were associated with two batches of High Flux Isotope Reactor (HFIR) fuel (Batches 11 and 13) being dissolved in dissolver 6.4D. The 640 nm laser was used for measurements associated with MTR Batch 22 and HFIR Batch 11; all other dissolutions were monitoring using the 532 nm laser. During these tests, the only molecular species observed were NO_2, H_2O, N_2, and O_2. Although N_2O, NO, and H_2 are known to be produced during aluminum alloy dissolution, these species were not observed with the Raman spectrometer. The specific reactions governing offgas chemistry between the dissolver and the sampling point are not known in enough detail to facilitate the conversion of the NO_2, N_2, and O_2 readings to an amount of material dissolved. However, NO_2 readings are believed to correlate with specific process events, and it is assumed that NO_2 may be used as a proxy for dissolver activity.

The NO_2 readings can be used as a process indicator. The ability to correlate the readings to fragment height measurements from post-run probing is proposed, although more data is required to validate the universal applicability of the correlation. Nonetheless, the tail end readings can be used to indicate that the fragment height has reached the threshold for the completion of a run, reducing the instances of an extended dissolution if the charge has been run for too short a time. Also, as the correlation between NO_2 readings and fragment height becomes more robust, time savings from the accelerated charging of bundles might be realized if the charging can be done earlier than the prescribed dissolution time.

Recommendations are made for increasing the integration of the offgas monitor into the facility. For the near-term these include establishing a reading(s) external to the trailer which can be used by engineering. Long term these include direct communication of the readings and instrument status to the Control Room, duplication of the instrument to allow simultaneous monitoring of both dissolvers, and potential improvements to the existing unit.

TABLE OF CONTENTS

LIST OF TABLES

LIST OF FIGURES

LIST OF ABBREVIATIONS

ABD	Accelerated Basin Deinventory
CCD	Charge Coupled Device
DRR	Domestic Research Reactor
EBS	Expanded Basin Storage
FRR	Foreign Research Reactor
HFIR	High Flux Isotope Reactor
LiDAR	Light Distance and Ranging
LOD	Limit of Detection
MTR	Material Test Reactor
NM	Nuclear Materials
PLS	Partial Least Squares
SNF	Spent Nuclear Fuel
SRNL	Savannah River National Laboratory
SRS	Savannah River Site

1.0 Introduction

1.1 Application

To reduce the stored inventory of Spent Nuclear Fuel (SNF) and Nuclear Materials (NM) at Savannah River Site (SRS), the SRS H-Canyon processing facility is pursuing an Accelerated Basin Deinventory (ABD) program that concentrates efforts on fuel dissolution and transfer to the Defense Waste Processing Facility for vitrification.[1] This approach places greater emphasis on the efficiency of the dissolving operations. Savannah River National Laboratory (SRNL) is supporting this change through the development of an alternate monitoring technique to determine the status of fuel bundle (Material Test Reactor, MTR) and fuel element (High Flux Isotope Reactor, HFIR) dissolution.[2] Two different techniques have been considered: Light Distance and Ranging (LiDAR) and Raman spectroscopy. A preliminary study of the suitability of LiDAR to detect fuel bundles protruding above the liquid surface (which can occur with MTR fuel bundles) inside the dissolver insert well has been completed.[3] This report describes the development of a monitor based on Raman spectroscopy to provide real time measurements of molecular components in the dissolver offgas stream, including NO_x, H_2, N_2, and O_2. These gases are characteristic of the dissolution process and their presence serves as a proxy indicator that material is still being dissolved. The hypothesis is that H-Canyon process engineers could possibly run individual dissolving charges for a shorter period of time, knowing from the Raman measurements that the dissolution period was complete when the proxy gases were no longer observed. Herein, the demonstration of the Raman instrument to monitor multiple charges of two types of SNF is presented.

SRNL has demonstrated the use of Raman spectroscopy to monitor gaseous products in several laboratory-scale experiments, including chemical[4, 5] and electrolytic[6] dissolution studies simulating H-Canyon operations. However, there are several important differences between those studies and in-facility monitoring that required additional instrument development. In the lab spectra, the gas peaks are sampled by only a few pixels on the array detector, due to a combination of detector design and less dispersion in the spectrometer. This undersampling reduced measurement consistency over a given run. Environmental conditions in the laboratory were more stable than field conditions, which exhibit a wide range of temperatures. Compensatory measures for instrument drift needed to be developed. Lab-based spectra were obtained with 532 nm excitation, but another wavelength may be a better choice (this is discussed in more detail below). Finally, a new gas flow cell was designed to improve light collection efficiency and ensure materials compatibility with the potentially acidic and radioactive gas stream.

Raman spectroscopy was chosen for this application due to its ability to measure all the molecular species of interest. In contrast, infrared absorbance measurements are insensitive to homonuclear diatomics such as H_2, N_2, and O_2. Raman spectroscopy's compatibility with optical fibers, due to the measurements being made with visible wavelengths of light, is another advantage compared to infrared. Fiber compatibility permits a more advantageous location for the instrument and reduces potential worker exposure to hazardous conditions. These advantages have been recognized by other DOE laboratories that have demonstrated the suitability of Raman-based gas monitoring in applications such as measurement of I_2 gas emitted from molten salt reactors[7] and trace gas detection in natural gas streams.[8] Raman spectroscopy has also been used for long term monitoring of hydrogen isotope distributions in the Karlsruhe Tritium Neutrino project.[9] However, to our knowledge this is the first report of the use of Raman spectroscopy directly in a nuclear fuel materials processing facility to monitor offgas constituents.

1.2 Dissolver chemistry

Hyder *et al.* have described the dissolution chemistry, offgas treatment, and other aspects of H-Canyon process operations for both chemical and electrolytic dissolutions.[10] A representative summary of the gas

generation and chemistry of the dissolvers, concentrating on chemical dissolution of aluminum-clad fuels, is as follows. The bulk of the reaction is associated with aluminum dissolution[11]:

$$Al + 3.75\ HNO_3\ (+\ Hg^{2+}\ catalyst) \rightarrow Al(NO_3)_3 + 0.225\ NO + 0.15\ N_2O + 0.11\ N_2 + 1.9\ H_2O + 190\ kcal/mol\ Al. \quad (1)$$

The above stoichiometry occurs at approximately 4M HNO_3. The amount of nitric acid consumed and the composition of the evolved gas (for example, the NO/N_2O ratio) vary with acidity in a manner consistent with the reducing strength of the solution[12], but the identities of the products do not change.

The stoichiometry of the dissolution of uranium in nitric acid is not thoroughly agreed upon[13] and may be dependent on the nitric acid concentration in the solution. Based on Ref. 13 the most likely reactions are either of the two listed below:

$$3\ UO_2 + 8\ HNO_3 \rightarrow 3\ UO_2(NO_3)_2 + 2\ NO + 4\ H_2O \quad (2a)$$
$$U + 4\ HNO_3 \rightarrow UO_2(NO_3)_2 + 2\ NO + 2\ H_2O \quad (2b)$$

NO_2 may be produced from NO via the reactions (at nitric acid concentrations < 6.7 mol L^{-1})[13]

$$2\ NO_{(dissolved)} + HNO_3 + H_2O \rightarrow 3\ HNO_2 \quad (3)$$
$$HNO_2 + HNO_3 \rightarrow 2\ NO_2 + H_2O \quad (4)$$

The gas passes through a condenser which recovers nitric acid through the conversion of NO_x gases[10,14]:

$$2\ NO + O_2 \rightarrow 2\ NO_2 \quad (5)$$
$$3\ NO_2 + H_2O \rightarrow 2\ HNO_3 + NO \quad (6)$$

Hyder does not report on the fate of N_2O in the condenser. Groves and Sasenow, in discussing NO_x and N_2O emission abatement from nitric acid plants, note that in the absence of catalytic oxidation, N_2O reactions do not occur in condensers.[15] The catalytic reactions noted in that article occur at temperatures of 250 °C or higher, which exceed gas temperatures achieved in the H-Canyon dissolution process.

The offgas is next directed through a heated reactor containing silver nitrate coated berl saddles, which trap radioactive iodine. A probable reaction is thought to be[10]:

$$6\ AgNO_3 + 3\ I_2 + 3\ H_2O \rightarrow 5\ AgI + AgIO_3 + 6\ HNO_3 \quad (7)$$

with the reactor maintained between 175 – 190 °C. Finally, the offgas passes through a particulate filter (steam-heated glass wool) before being emitted from the stack.

The Raman sampling point for the offgas occurs after the particulate filter, as described in Section 2.1.

Another factor in the consideration of the chemical composition of the offgas is the solubility of the dissolution products in the nitric acid solutions. Both N_2O and NO have limited solubility in nitric acid, but NO_2 (or more specifically the dimer N_2O_4, which is present in an equilibrium with NO_2) readily absorbs in nitric acid solutions[16,17]. This results in a baseline NO_2 presence in the offgas stream when the solution is sparged and purged.

1.3 Processing details

Two types of aluminum-clad SNF were dissolved during these observations, MTR and HFIR fuel. MTR bundles contain assemblies which are either Foreign Research Reactor (FRR) or Domestic Research

Reactor (DRR) SNF. The fuels differ in their dimensions. MTR assemblies varies in length and cross-section shape. The shape of the assembly can be square, rhombic, pie, etc. The assemblies can also be nested cylinders. MTR assemblies are stored in L-Bundles, also known as Expanded Basin Storage (EBS) bundles. An L-Bundle is approximately 11.5 feet long and 5 inches in diameter and typically contains 4 – 8 MTR assemblies. HFIR fuel consists of nested cylinders called elements. The outer element is approximately 31" long and has an outside diameter of approximately 17" and an inner diameter of approximately 11". The inner element is approximately 31" long and has an outside diameter of approximately 10.5" and an inner diameter of approximately 5". Due to these shapes and sizes, different dissolver inserts are required to provide and maintain spacing during the dissolution process (the spacing for MTR is required for criticality safety). H-Canyon has two different size dissolvers. MTR is dissolved in the smaller 6.1D dissolver and HFIR is currently dissolved in 6.4D dissolver. (Due to process efficiencies, MTR could be dissolved in 6.4D, but HFIR would not be dissolved in 6.1D.) Within a batch run, multiple fuel loadings ("charges") are put into the same nitric acid solution before the solution is transferred to a storage tank. When this testing was initiated, an MTR run had three charges, with 3, 4, and 5 bundles successively in each charge to dissolve 12 bundles. H-Canyon has switched to a new flowsheet which allows 12 bundles to be dissolved using on only two charges of 6 bundles. MTR Batch 26 evaluated herein used the revised flowsheet. A HFIR batch has five charges, each with a single core of one inner and one outer element.

The rough sequence of operations for dissolution, after the fuel is retrieved from storage, is first to place the fuel in the insert, which is partially submerged in nitric acid for MTR and completely submerged for HFIR and seal the dissolver. The dissolver is maintained at a slight negative pressure as part of the contamination control strategy. Startup begins with heating the solution through the introduction of steam to heating coils, introducing sparge and purge air, and adding mercury as a catalyst (first charge only – the mercury remains viable for all subsequent charges in a batch). For MTR, as the submerged bundles and assemblies dissolve, the remaining material above the liquid level slides into the solution by gravity. The time allowed for complete dissolution increases with each charge introduced, i.e. 36, 44, and 54 hours for the 3, 4, 5 charging sequence and 50 and 60 hours for the 6, 6 charging sequence for MTR, and 28, 32, 40, 50, and 60 hours for HFIR. After the prescribed time, steam to the coils is turned off and cooling water is applied to the coils to cool the dissolver. Once the dissolver is cooled, the inserts are mechanically probed to determine the height of any undissolved material present. If remaining material is found to be in excess of a predetermined limit, an extended dissolution is performed by resealing and reheating the dissolver for 12-24 hours. The dissolver is then cooled and re-probed to confirm that fragments are at an acceptable level.

There are two scenarios whereby a high probe measurement can be obtained. The most common scenario, applicable to both the MTR and HFIR dissolution, is that material has been submerged but is not completely dissolved. The time allotted for the dissolution process is based both on processing history and flowsheet development studies that define expected variations in dissolution acidity, aluminum nitrate concentration, cladding metallurgical properties, mercury catalyst concentration, and other factors that can influence the dissolution rate.[18,19] One hypothesis for material not dissolving in the allotted time that is relevant to the MTR process is that the sliding of the bundles inside the insert well into the dissolvent may not always be a continuous process, and material may be held up in the insert well for a period of time before collapsing into the nitric acid. Furthermore, the bundles have a special more robust end cap to allow them to be loaded into the inserts with cranes. These end caps differ from the assembly cladding in Al alloy composition and temper and have been shown to dissolve more slowly in nitric acid.[20] A late introduction of this material into the dissolvent could result in incomplete dissolution at the end of the prescribed time. Regardless, of what part of the bundle is contributing to the residual fragment, the Raman measurement is intended to detect the presence of fragments in the dissolvent via the observation of chemical constituents in the offgas that are characteristic of the dissolution process.

The less common scenario that is only applicable to MTR dissolution is that the bundle material becomes wedged in the insert and never reaches the dissolvent. The probing action knocks this material loose causing it to fall into the solution. Because the material was never exposed to the dissolvent, its presence in the insert did not lead to gas generation. Therefore, this scenario cannot be detected with the Raman monitor. The investigated use of the LiDAR prior to probing is intended to detect unsubmerged material in this scenario. The feasibility of converting integrated Raman offgas measurements and gas flow rates to the quantity of material dissolved is explored in Section 3.3.5.

The potential of Raman offgas monitoring to improve process operations addresses two situations. One occurs when the dissolution has occurred smoothly and all submerged material has been dissolved sooner than the allotted time. If the monitoring indicates that characteristic offgases are no longer being produced, the dissolver can be cooled earlier, accelerating the transition to the next charge. The other case is if at the end of the allotted time, there is material remaining in the well in excess of the acceptable amount. If this condition is suspected, the facility could move immediately to extend the dissolution period without the time and effort associated with shutting down and restarting the dissolver (cooling the dissolver, uncovering the canyon cell, removing the dissolver lid, probing, reinstalling the lid, recovering the canyon cell, and reheating the dissolver). Estimates of the time savings available for both cases will be presented in Section 3.3.3.

1.4 Raman spectroscopy

A discussion of the basic principles of Raman spectroscopy is warranted to explain some observations related to the measurement of NO_2 gas. The Raman effect is the inelastic scattering of light from a material, as the frequency of the scattered light differs from the frequency of the incident light. It is most easily observed when the incident light is intense and of a single frequency, as is provided by a laser. The frequencies of the Raman scattering are characteristic for each molecule and correspond to the vibrational and rotational frequencies of the molecule. The intensity of the Raman scattering is dependent on the laser power, the concentration, and the intrinsic ability (known as a "cross-section") of the molecule to produce Raman scattering from a given excitation frequency.

The cross-sections depend on the coupling between the electronic states that are excited by the incident laser and the vibrational/rotational states involved in the Raman scattering. For most gas molecules (including H_2, N_2, O_2, NO, and N_2O, which are possibly present in the samples monitored here), the energies of the electronic states greatly exceed the energy of the laser wavelength. The excitation is considered "non-resonant", meaning that the laser energy is not preferentially coupled into a specific electronic state. Under non-resonant conditions, the choice of laser frequency does not change the Raman scattering cross-section. From a practical perspective, a calibration for the concentration of these gases, based on the measurement of multiple peaks, will not depend on the laser frequency chosen. Likewise, drifts in the laser frequency that may occur under changes in ambient conditions will not lead to a drift in the derived results.

In contrast to the gases mentioned above, which are colorless, NO_2 is a red-brown gas that strongly absorbs light at 532 nm (green) and weakly absorbs it at 640 nm (orange). The absorption profile of NO_2 is shown in Figure 1-1.[21,22] The absorption of light is associated with the excitation of specific electronic/vibrational/rotational states in the molecule. These two wavelengths access different states, with different coupling to vibrational states in the ground electronic state. The Raman scattering cross-sections for NO_2 will change for these two laser wavelengths, and thus the Raman spectra and NO_2 concentration calibrations will also vary. As can be seen in Figure 1-1, there are many sharp peaks within the absorbance spectrum, and some variation in the Raman spectrum may be observed if the laser frequency is detuned from resonance with one of these peaks.

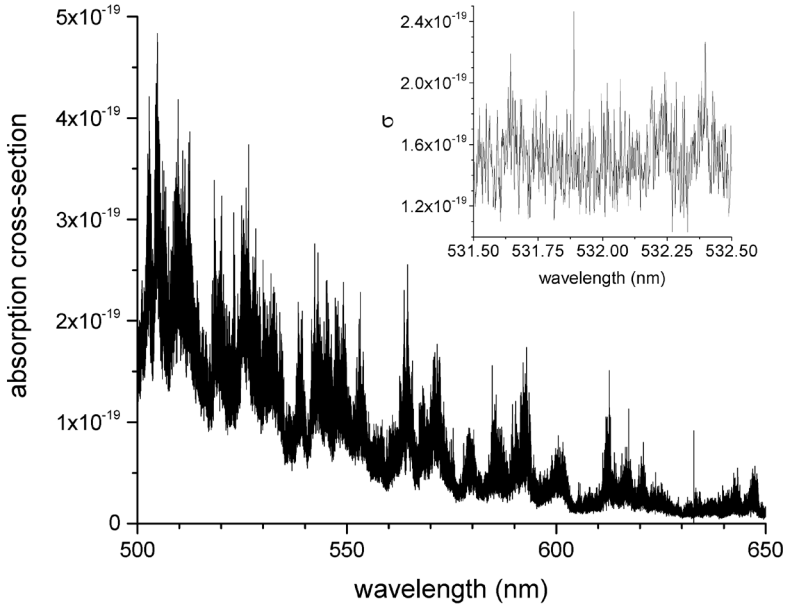

Figure 1-1. Absorption spectrum of NO_2 at 294K.

(From Ref. 22)

NO_2 Raman measurements are further complicated due to the competing effect of resonant molecular fluorescence that also occurs upon excitation, especially with 532 nm light.[23] The relative strengths of the Raman scattering and fluorescence emission depend on sample pressure, with increasing pressure reducing fluorescence due to quenching effects. The tradeoff of using the 532 nm versus the 640 nm laser light to generate the Raman signal is seen in these effects. The measurement at 532 nm can potentially detect lower concentrations of NO_2 due to resonance Raman excitation or even resonance fluorescence emission. However, the magnitude of these effects may be particularly sensitive to measurement conditions (sample pressure, temperature-induced laser drift) and thus the measurements at 640 nm may be more stable. During these test runs, measurements were made with both laser wavelengths in order to determine the best selection for future use.

2.0 Experimental Procedure

2.1 Instrumentation

The Raman instrument is assembled from commercially available components.* The general scheme is shown in Figure 2-1, and an annotated picture of the installed unit is shown in Figure 2-2. Light from a solid state diode laser is coupled into an optical fiber. At any one time, either a 532 nm (green) laser (300 mW power) or a 640 (orange) nm laser (500 mW) was used. (The laser used to monitor a particular charge is noted in the discussion of the monitoring results in Section 3.) After emerging from the other end of the fiber, the light is collimated, passed through a 45° bandpass filter to remove Raman scattering generated by the fiber material, and focused into a gas cell. Raman signal from the sample is collected in the backscattering geometry, reflected by the bandpass filter (removing the bulk of the Rayleigh-scattered excitation light), and focused into a 6-around-1 fiber bundle. At the other end of this bundle, the seven fibers are arranged in a vertical row oriented to match the entrance slit of the spectrometer. The wavelength-

* Spectrometer: iHR 320, f/4.1, 0.32 m (Horiba). 600 mm^{-1} grating. Detector: Syncerity 2048x512-NIR (Horiba), -75 °C. Laser: LPX-640 (Oxxius), 640 nm, or Duetto532 (RMPC Lasers), 532 nm. Optical filters: StopLine notch filter, RazorEdge dichroic filter, and RazorEdge long-pass edge filter at appropriate wavelengths (Semrock). Lenses: Edmund Optics. Optomechanics: ThorLabs.

dispersed light is detected by a cooled charge-coupled device (CCD) detector (2048 pixels horizontal x 70 pixels vertical). The spectrometer and detector are controlled with a hybrid program that utilizes manufacturer drivers and communications protocols controlled by Visual Basic macro programs operating within an Excel spreadsheet written at SRNL.

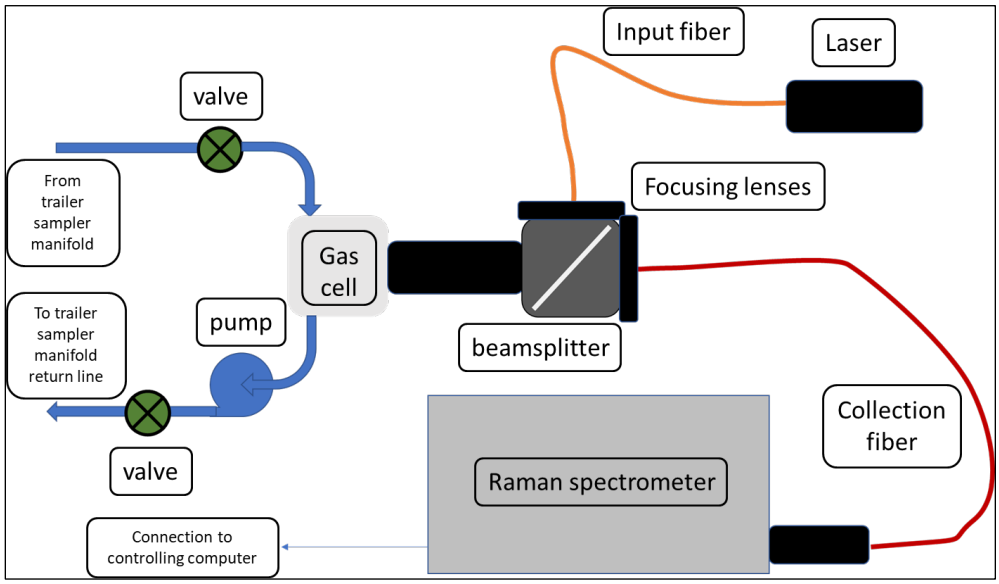

Figure 2-1. Schematic diagram of Raman instrumentation.

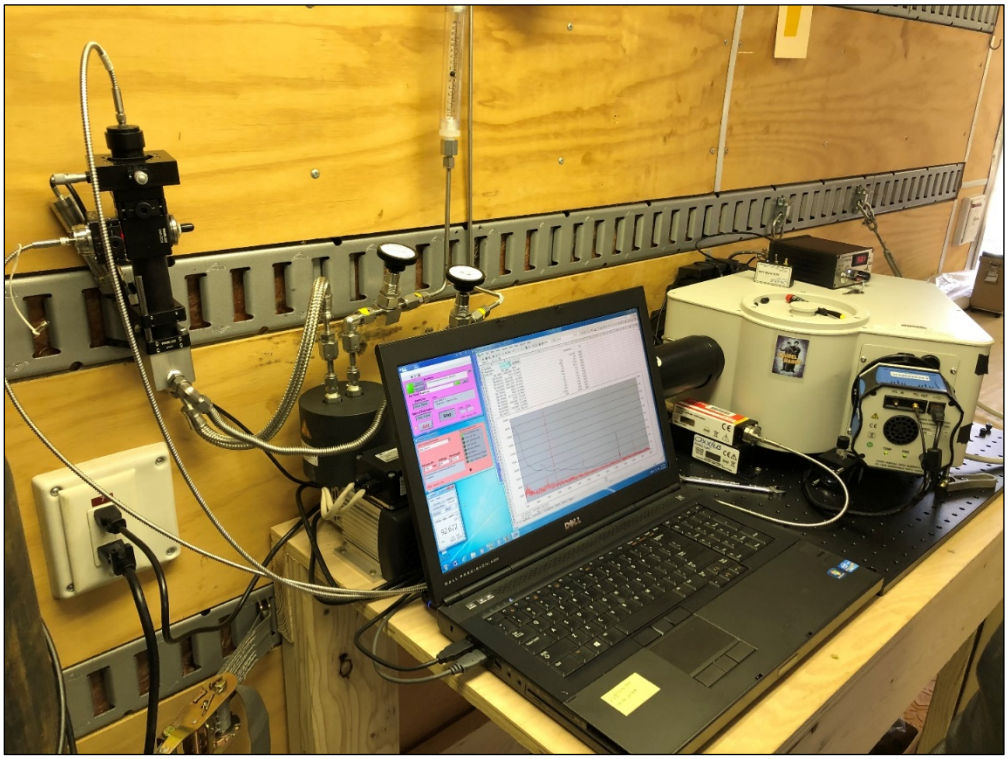

Figure 2-2. Raman instrumentation in the analytical trailer.

The focusing optics and gas cell are shown in Figure 2-3. All components are arranged using a commercially available optical cage mount system for ease and consistency of alignment. The cage mount relies on four parallel rails and a set of optics holders that slide onto the rails via precisely positioned holes to maintain concentric and parallel alignment. The gas cell was constructed by SRNL from a machined steel block, with a volume of approximately 30 mL. Gas inlet/outlet lines are braided stainless steel, with pipe thread connections to the block and adapters allowing the use of compression fittings for the lines. The gas cell does not incorporate any retroreflection optics, waveguides, or other means to extend the sampling volume or improve collection of the Raman signal.[8,24,25] These improvements were not necessary for the present application but could be added if required.

The equipment and cell are located in an analytical trailer located outside H-Canyon. An external manifold allows for connection to the exhaust lines associated with the 6.1D or 6.4D dissolver. The analytical trailer has a single gas input line. Switching between the two facility lines is simple but requires line breaks and therefore facility support. The sampled gas stream is hot, condensing, and potentially radiologically contaminated and must be conditioned. The external manifold includes a condensation pot to reduce the moisture content, which is needed to reduce the risk of inaccurate measurements associated with moisture condensation on the cell windows.[*] The dried stream passes through a HEPA filter to remove particulates and reduce potential radiological contaminants. The trailer has a pump to ensure the offgas is adequately pulled through the manifold and into the trailer. Once in the trailer, the primary gas stream is split into several secondary lines dedicated to various instruments. The Raman instrumentation includes a secondary pump to maintain good sample exchange and flow. Wetted materials in the pump and fittings are temperature and corrosion resistant. The pump is vibrationally isolated from the rest of the equipment through the use of flexible stainless steel tubing.

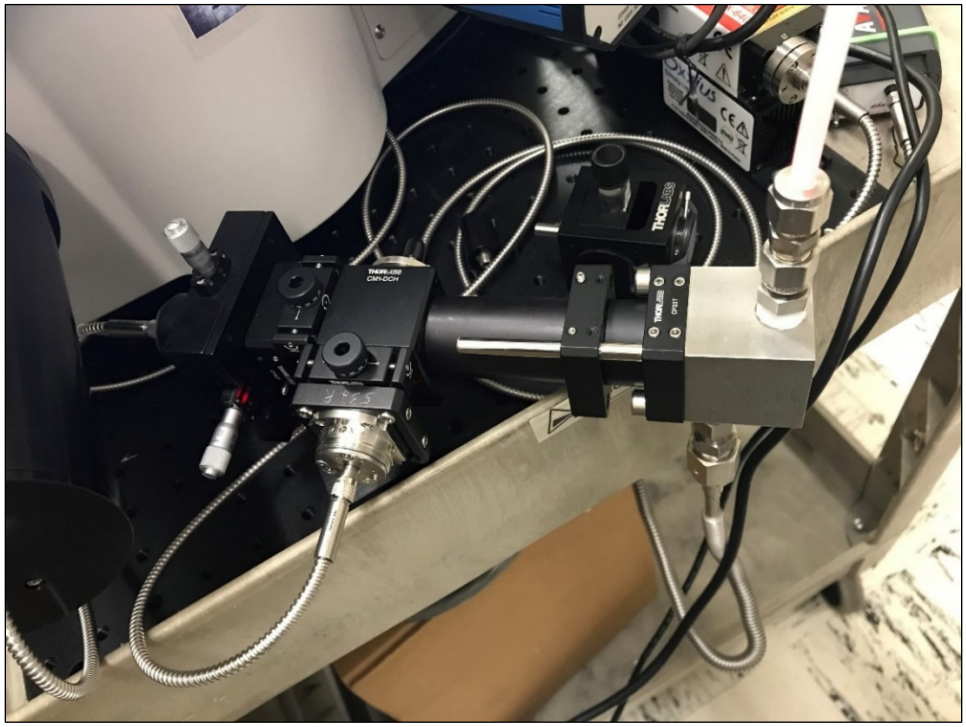

Figure 2-3. Raman gas cell and collection optics.

[*] Periodically, the pot is emptied by pumping the trapped liquid back to the exhaust line. Sampling of the liquid showed it to be brown and highly acidic, consistent with a high concentration of nitric acid and dissolved NO_2.

2.2 Calibrations and Data Processing

An initial wavelength calibration of the spectrometer is achieved by setting the orientation of the spectrometer grating and measuring the positions on the CCD detector array of the emission lines from a neon pen lamp. Typical instrument settings and spectral parameters are shown in Table 2-1. In the table, "spectral range" refers to range of Raman shift values (in wavenumbers) covered with the choices for laser wavelength, grating line density, and center wavelength setting for the spectrometer. These settings, combined with the high pixel density of the detector, allow the narrow gas peaks to be sampled with multiple pixels (for example, approximately 13-15 pixels for N_2 in clean air measurements) and make the measurements more stable. The acquisition time (in seconds) is the amount of time that light is allowed to fall on the detector before readout.

Table 2-1. Spectral acquisition parameters.

Laser wavelength (nm)	Grating line density (mm^{-1})	Slit width (μm)	Center wavelength (nm)	Spectral range (cm^{-1})	Acquisition time (s) and averages	Readout rate (kHz)	CCD sensitivity	Approx peak FWHM[a] (cm^{-1})
532	600	69	608	365-4130	10, 6x	45	High	8
640	600	69	720	385-3022	60, 6x	45	High	6

(a) FWHM = Full Width at Half Maximum; determined from the 2331 cm^{-1} N_2 line.

Raman spectra are based on the frequency shift between the exciting laser and the scattered light. These shifts, expressed in wavenumbers (reciprocal wavelength, cm^{-1}), are independent of the wavelength of the exciting laser. An initial wavenumber calibration is obtained by the measurement of cyclohexane liquid, a commonly used standard for this purpose.[26] The liquid is contained in a square-sided, sealed cuvette, and the cuvette is mounted in a holder that is compatible with the cage-mounting system described above. The cuvette holder can be manually swapped with the gas cell without misaligning the rest of the optical path. Once the instrument was calibrated against the cyclohexane shift standard, the cuvette holder was replaced with the gas cell. Continued validation of the instrument was made against air (N_2, O_2).

The temperature changes experienced by the instrument cause a linear shift in wavenumber across the spectrum. These shifts are determined in real time by the automated identification of the N_2 peak at 2331 cm^{-1}, as that gas is expected to be present at all times and does not overlap Raman lines for other expected gases. All spectra are automatically shifted by the data acquisition software macro to restore the correct position of the N_2 peak before additional processing is carried out. A detailed demonstration of the automated correction is presented in Section 3.2.3. After this correction, the spectra are interpolated to a predefined grid of shift values from 300-3300 cm^{-1}, with points spaced by 1 cm^{-1}. This common basis allows for the consistent application of the gas concentration fitting models.

The process for calibrating spectral data to yield gas concentrations has been described previously.[27] Spectra are smoothed and processed to the second derivative. Molecular response functions are determined for each analyte by assuming Gaussian peak shapes and line shifts, intensities, and widths. A spectrometer response function is determined to account for variations in grating efficiency, detector response, and other factors. Integration time and laser power provide linearly proportional changes to signal intensity but affect all peaks equally. The absolute Raman signal is also proportional to the sample line pressure, which was observed to vary between 75-95 kPa. To compensate for variations in laser power and system pressure, the measured concentrations were normalized to the sum of the components which were detected in the stream (for this application, N_2, O_2, and NO_2).

2.3 Quality Assurance

Requirements for performing reviews of technical reports and the extent of review are established in Manual E7 2.60. SRNL documents the extent and type of review using the SRNL Technical Report Design Checklist contained in WSRC-IM-2002-00011, Rev. 2.

3.0 Results and Discussion

3.1 Process Run History

Two complete MTR batches (Batches 22 and 24), one partial MTR batch (Batch 26), one complete HFIR batch (Batch 11), and one partial HFIR batch (Batch 13) were monitored. Table 3-1 summarizes these runs, including process notes and other comments.

Table 3-1. Process runs monitored.

Campaign / Batch	Charge	Date	Raman Laser	Comments
MTR #22	1	12/28-29	640 nm	3 bundles. Probe measured <4". Dissolver not fully sealed (all charges).
	2	2/6-7		4 bundles. Probe measured <4". Problems maintaining vacuum on dissolver, and air intake was likely.
	3	2/20-22		5 bundles. Ran for 28 hours and stopped due to low liquid level - 24" probe, Well #2; 4" probe, Wells #4, #6, #8, #10. On restart, continued dissolving for 26 more hours. Probe measured <4".
MTR #24	1	4/18-4/20	532 nm	3 bundles. 5" probe, Well #8. Dissolver not fully sealed (all charges). Extended dissolution completed.
	2	4/21-4/23		4 bundles. Probe measured <4".
	3	4/24-4/27		5 bundles. 5" high probe, Well #2. Extended dissolution completed.
MTR #26	1	6/5-6/7	532 nm	6 bundles. Probe measured <4". Dissolver fully sealed.
	2	*8/7-8/9*		*(Data not collected due to instrument malfunction.)*
HFIR #11	1	2/25-2/26	640 nm	Probe measured >10" (estimated at 24"). Dissolver fully sealed. Extended dissolution completed. Probe measured 4.5".
	2	2/28-3/2		7" probe (not "high")
	3	3/13-3/15		1" probe (not "high")
	4	3/17-3/19		3" probe (not "high")
	5	3/20-3/23		No fragments detected.
HFIR #13	1	5/28-5/30	532 nm	7.5" probe (not "high"), one well. Dissolver fully sealed.
	2	5/30-6/1		5" probe (not "high"), one well.
	3	6/1-6/4		Steam turned off mid-run for approx. 13h. No fragments detected.
	4	*n/a*		*(monitor switched to MTR batch 26)*
	5	*n/a*		*(ibid.)*

3.2 Raman Measurements in H-Canyon

3.2.1 Characteristics of offgas spectra

Figure 3-1 shows Raman spectra of dissolver offgas obtained prior to processing, (black curve), during the peak of the emission (red curve), and near the end of the dissolution (blue curve). These processing states were confirmed by comparison of the time stamps of the spectra with the processing logs. The spectra are

offset for clarity. Prior to processing, the expected constituents of the gas stream are N_2 and O_2. The peaks corresponding to these species, at 2331 and 1556 cm^{-1}, respectively, are labeled in Figure 3-1. There are also several peaks that are due to Raman scattering from the cell windows. These signals are a regular background for the cell, but fortunately do not interfere with any of the analytically sensitive lines.

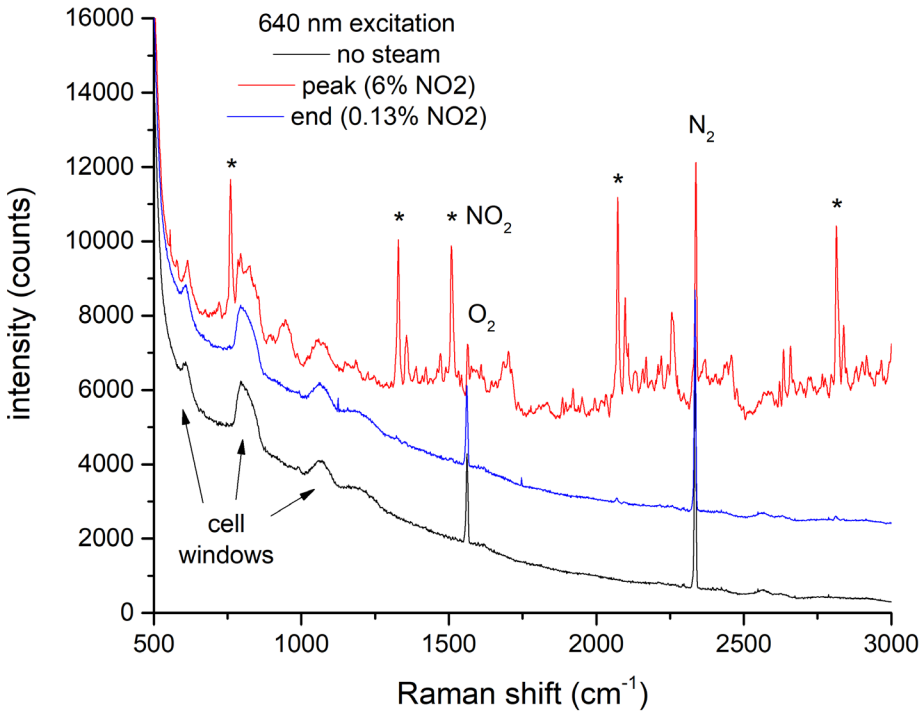

Figure 3-1. Typical Raman spectra at various times during a process run.

The spectrum at the peak of the dissolution shows a multitude of lines in addition to those from air. These are almost entirely due to NO_2, with the most analytically useful peaks denoted by asterisks in Figure 3-1. As noted in Section 1.2, NO_2 is a minor aluminum dissolution offgas species. The prominent peaks for the major offgas products N_2O, NO, and H_2 are not seen.* For 640 nm Raman spectra, 5 lines are used to quantitate NO_2: 751, 1321, 1501, 2065, and 2808 cm^{-1}, as denoted in Figure 3-1 by asterisks. Bands due to H_2O are seen at ~1650 and 3200-3400 cm^{-1}. Although the spectrum at the end of the dissolution looks mostly like the spectrum of air, there still are signatures associated with NO_2. This is seen more clearly when the scale is expanded, as shown in Figure 3-2. Although small, these bands still provide statistically meaningful information, as discussed in the following section.

The spectra taken in Figure 3-1 and Figure 3-2 were taken with 640 nm excitation. As discussed in Section 1.4, the spectra are expected to change with 532 nm excitation due to the resonance excitation conditions of NO_2. This is demonstrated in Figure 3-3, which compares spectra obtained with both excitation wavelengths, demonstrates this to be the case. The spectra were taken during the peak emission of offgas from the first charges in HFIR Batch 11 (640 nm) and 13 (532 nm) and should be roughly comparable with respect to dissolver conditions. The larger signals for the spectra obtained at 532 nm excitation are obtained despite a shorter integration time (10 s versus 60 s for 640 nm). The 532 nm spectrum is not a simple multiplication of the 640 nm spectrum. Instead, new peaks appear, changing the shapes of some of the

* Expected peak positions include: N_2O, 1284 and 2222 cm^{-1}; NO, 1876 cm^{-1}; and H_2, 352, 586, 813, 1034, and 4155 cm^{-1}.

peaks used for NO_2 calibrations with 640 nm excitation (1321, 2065, and 2808 cm^{-1}). The NO_2 peaks observed to be less affected by these changes are at 751 and 1501 cm^{-1}. Therefore, NO_2 calibrations for

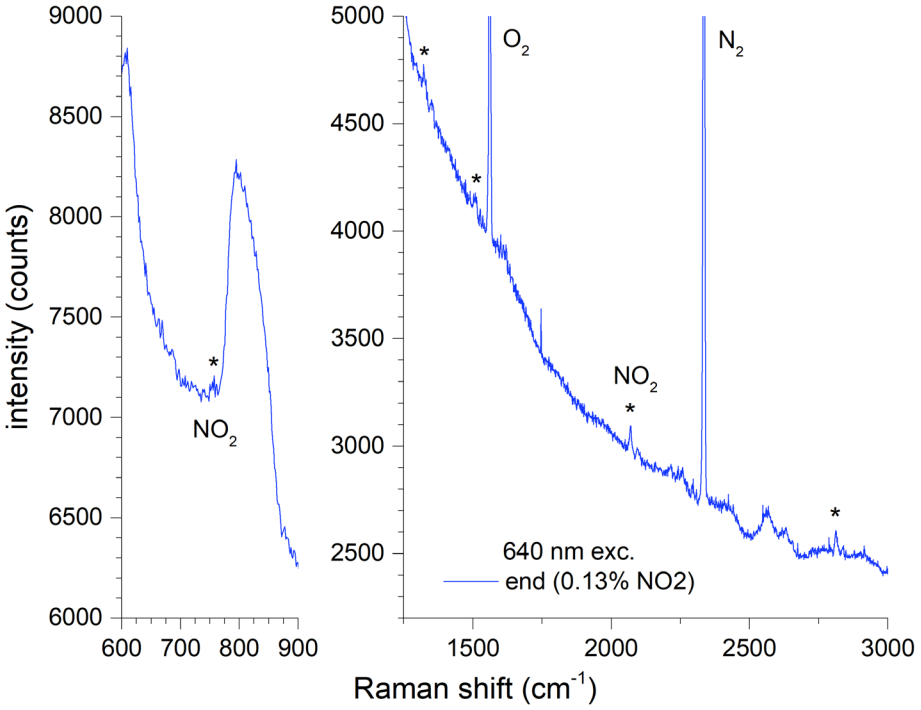

Figure 3-2 Expanded Raman spectrum of trace NO_2 in air.

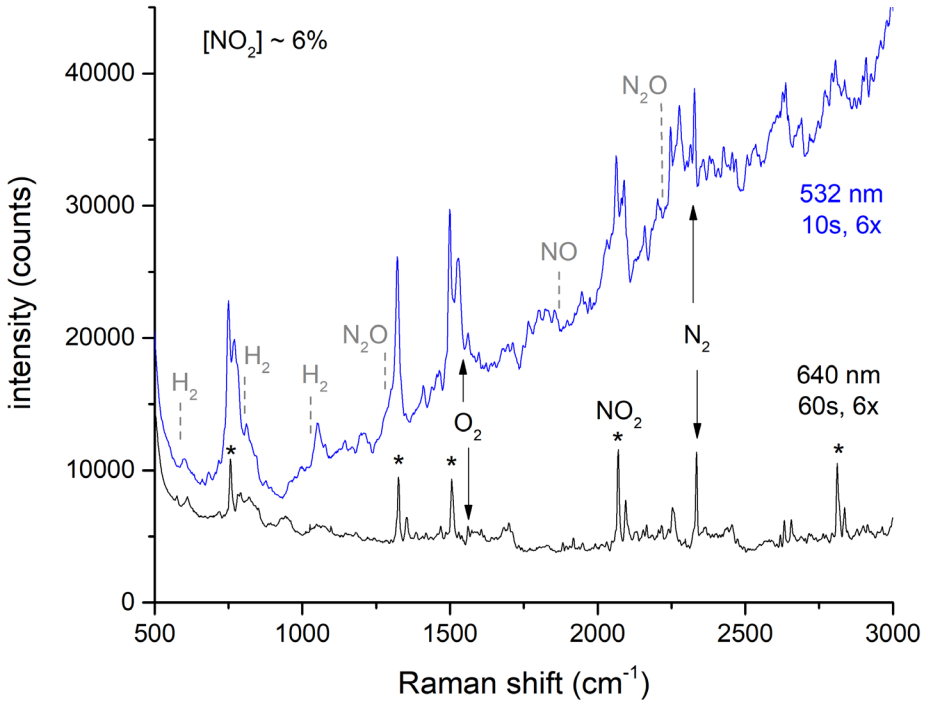

Figure 3-3. Dependence of Raman spectra on excitation wavelength.

spectra obtained at 532 nm excitation are based solely on these two peaks. The new peaks also overlap with the expected positions for NO and N_2O, as indicated in the figure. As a result, the detection limits for those species may be higher than with 640 nm excitation. This possibility is explored in the next section.

3.2.2 Detection limits and measurement precision

A classic definition of the limit of detection (LOD) for an analytical method is 3 times the standard deviation of the measurement for a large number of blank samples where the analyte is not detected and the conditions are representative of process measurements. As demonstrated in Figure 3-1, the gas stream before and at the end of a charge is essentially the same, except for a trace amount of NO_2 being present in the tail. Therefore, measurements before a charge with no detectable NO_2 are suitable for the calculation of the LOD. The observed LODs were 0.028% at 532 nm excitation and 0.037% at 640 nm excitation.* The improved LOD for 532 nm excitation is consistent with the increased sensitivity at that wavelength due to resonance enhancement and the intrinsic λ^{-4} dependence of Raman intensity on excitation wavelength. This is partially counterbalanced by the lower power of the 532 nm laser. Regardless, both laser wavelengths provide adequate sensitivity to observe NO_2 in the offgas stream at the tail end of the dissolution, as will be shown in Section 3.3.

For the other gas species of interest – N_2O, NO, and H_2 – separate detection limits can be defined for air and for the conditions during peak dissolution. These conditions are distinct because the Raman and fluorescence scattering from NO_2 generate a large background that interferes with the Raman signal of the other species. Table 3-2 shows the LODs under these conditions. Here, the peak emission is defined to be when the $\%NO_2$ reading exceeds 1%. During peak emission, the LODs for these other species are higher. They are also higher with 532 nm excitation, where NO_2 signals are more intense and have a stronger interference effect. This factor outweighs the λ^{-4} intensity dependence described above.

Table 3-2. Limits of Detection (LOD) for N_2O, NO, and H_2.

	In Air		At Peak Emission	
Species	**LOD (532 nm)**	**LOD (640 nm)**	**LOD (532 nm)**	**LOD (640 nm)**
N_2O	0.25%	0.21%	0.85%	0.37%
NO	1.17%	0.66%	6.4%	2.5%
H_2	0.54%	0.47%	0.61%	0.55%

(a) Units: % of composition.

This analysis assumes that N_2O, NO, and H_2 are not present during peak emission. To validate this assumption, a high quality spectrum was constructed by averaging 112 spectra from the peak ($\%NO_2$ > 0.6%) emission of HFIR Batch 11, Charge 5. Spectra were taken with a 640 nm laser, generating the smallest background from NO_2 emission. This averaged spectrum is shown in Figure 3-4. The plots show the expected positions of the lines for these species. There is no visual evidence for lines associated with H_2 or N_2O. The 1876 cm^{-1} NO peak is coincident with a small NO_2 line; however, the intensity ratio of this peak to nearby NO_2 peaks is consistent with ratios observed for spectra of NO_2 by itself. Thus, there is no visual evidence for the NO peak. This coincidence of lines is one important reason for the comparatively large LOD for NO compared to other species. Assuming that the LOD improves with the square root of the number of averages, the absence of evidence for N_2O, NO, and H_2 in this highly averaged spectrum suggests that the concentrations of those species during peak dissolver emission are no greater than $1/\sqrt{}$ 112 = 0.094x the LODs shown in Table 3-2.

* For 532 nm, NO_2 was measured at 0.008% ± 0.0095% (1σ) for a 24-hour period on 5/27-28/21. For 640 nm, NO_2 was measured at -0.008% ± 0.012% for a 8-hour period on 3/13/21.

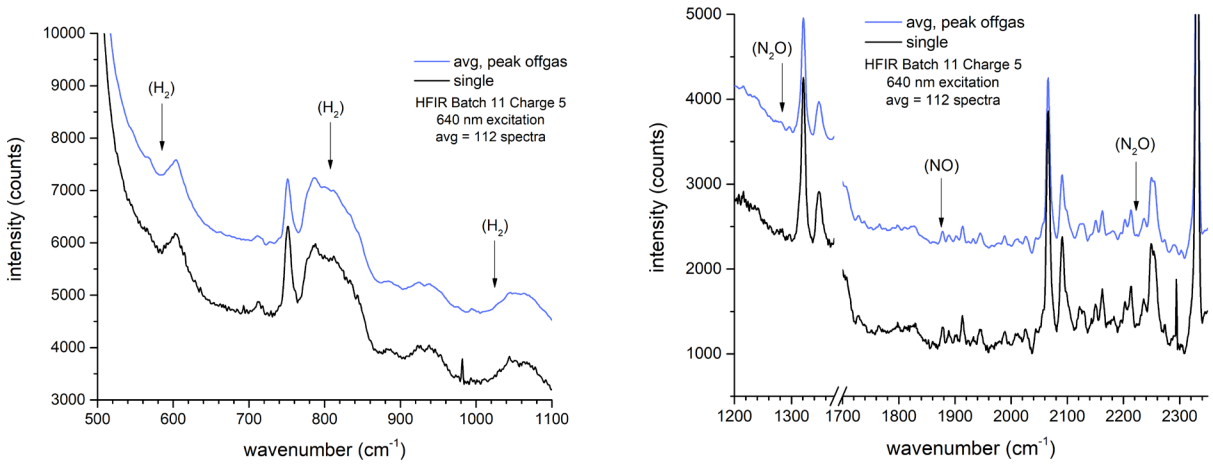

Figure 3-4. Absence of offgas components in averaged spectra during peak gas emission.

Measurement accuracy and precision can be assessed in several ways. First, air is a *de facto* standard for N_2 and O_2. Neglecting argon (which cannot be detected with the Raman measurement) and water, dry air is comprised of 78.8% N_2 and 21.2% O_2. For air measurements after installation, at 532 nm, N_2 = 78.53% ± 0.42% (0.5% of reading) and O_2 = 21.42 ± 0.34% (1.5% of reading). At 640 nm, N_2 = 78.13 ± 0.26% (0.3% of reading) and O_2 = 21.83 ± 0.25% (1.1% of reading). The superior precision of the N_2 measurements is consistent with the larger intensity of that peak in these spectra, and both uncertainties are consistent with the uncertainties noted in Ref. 27. The results show that lab calibrations can be successfully ported to process measurements. Second, the accuracy of NO_2 measurements from lab calibrations is estimated at 8% of the reading, consistent with uncertainties for other species such as CO_2 and N_2O at similar signal levels. Note that for there was no provision for introducing NO_2 gas standards for measurements in the trailer. However, the precision during a dissolver run can be assessed by observing measurement variations over a short period of time during which the expected concentration should be slowly varying (for example, for concentrations of 0.15-0.20% during the tail of the gas evolution). In these situations, at 640 nm, the precision was 5.4% of the reading (1-sigma) and at 532 nm, the precision (1-sigma) was 3.4% of the reading. The trend of improved precision at low concentration is consistent with the observed improvement of LOD on using 532 nm excitation.

The results indicate that both 532 and 640 nm excitation are adequate for measuring NO_2 in dissolver offgas streams. In Section 3.3.1 it is shown that changes in $\%NO_2$ correlate with changes in process conditions, and that the $\%NO_2$ reading is a suitable proxy for monitoring dissolver operations. Excitation at 532 nm provides greater sensitivity for NO_2 than 640 nm excitation, but the resonance excitation enhancement is sensitive to experimental measurement conditions. Thus, 640 nm excitation yields a more consistent measurement over possible environmental variation and is a more reliable choice for long-term use. Further, as noted above, reduced interference from resonantly enhanced NO_2 scattering permits more sensitive measurement of other species.

3.2.3 Instrument drift corrections

Changes in ambient conditions can lead to instrument drift. The Raman spectrometer was housed in a small trailed outside H-Canyon. Despite the use of two small air conditioners, temperatures inside the trailer routinely fluctuated due to changes in outside temperature and cloud coverage. These changes led to diurnal

drifts of Raman peak positions, as shown for N_2 in the bottom part of Figure 3-5.* This drift was automatically compensated with the wavenumber correction method described in Section 2.2. The need to make the correction is demonstrated in the top part of Figure 3-5. Uncorrected, the instrument cannot reliably measure $\%N_2$ in air, as the N_2 peak drifts out of alignment with the molecular response function. The correction restores the peak position and stabilizes the $\%N_2$ measurement.

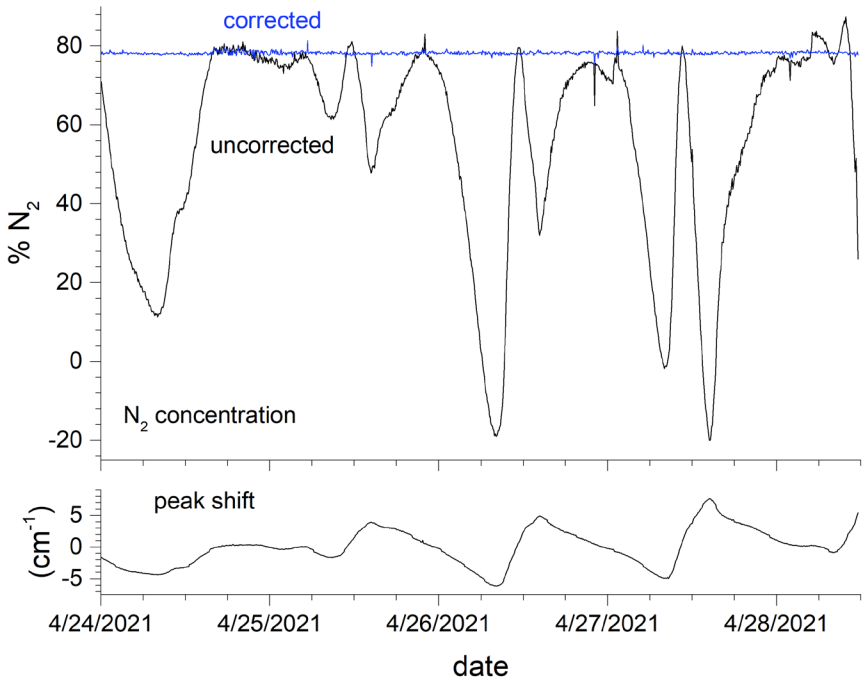

Figure 3-5. Effect of uncorrected instrument drift on N_2 measurements in air.

3.3 Process Monitoring Results

3.3.1 Gas evolution profiles

A typical time trace for the species NO_2, N_2, and O_2 in the offgas during a dissolver run is shown in Figure 3-6. (A full set of the evolution profiles for the runs listed in Table 3-1 is provided in Appendix A.) The changes in $\%NO_2$ correlate with the occurrences of significant process operations listed in Table 3-3. Starting from ambient conditions, there is no detectable NO_2 generated, and the offgas profile matches air. As the steam is turned on and the dissolver solution is heated, NO_2 generation begins. For the first charge in a batch, mercuric nitrate catalyst is added, accelerating the dissolving process and further increasing NO_2 production. For the second and subsequent charges in a batch, the mercuric nitrate catalyst from the first charge is already in place and the reaction accelerates to its maximum upon heating alone. Occasional spikes in NO_2 production are observed in MTR runs (for example, see 4/19/21, 0200 in Figure 3-6). The origin of the spikes is not known but may be due to material hung up in the dissolver inserts coming loose and falling into the liquid. The coincidence of $\%NO_2$ readings and process operations demonstrates that the $\%NO_2$ measurement is a suitable marker for tracking fuel dissolution.

* Dates and area temperatures (high/low, °F) over this period were: 4/24/21, 67/57; 4/25/21, 78/61; 4/26/21, 80/57; 4/27/21, 84/57; 4/28/21, 85/62.

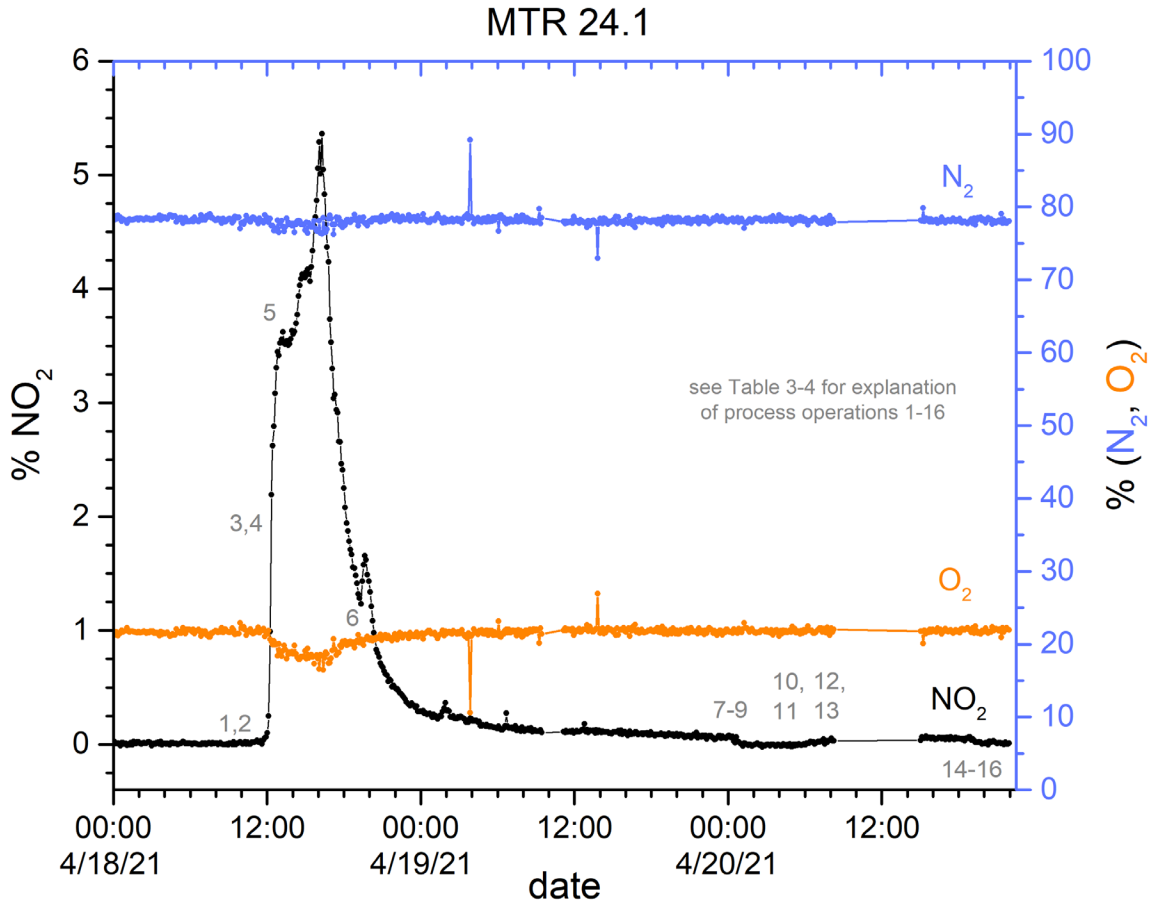

Figure 3-6. Evolution of process gases for MTR Batch 24, Charge 1

Table 3-3. Process operations for MTR Batch 24, Charge 1.

Event	Description	Event	Description
1	Sparge turned on	*probed high, extended dissolution required*	
2	Steam introduced	10	Sparge turned on
3	Dissolver reached boiling	11	Steam introduced
4	Switched sparge to purge	12	Reached boiling
5	Mercury addition initiated	13	Switched sparge to purge
6	Mercury addition completed	14	Dissolution completed, steam stopped
7	Steam stopped	15	Switched purge to sparge
8	Switched purge to sparge	16	Air sparge control valve closed
9	Air sparge control valve closed		

3.3.2 Endpoint detection.

Figure 3-7 expands the evolution profile to show the tail end of the dissolution shown in Figure 3-6. For this run, the primary dissolution was stopped after the prescribed time. Probing indicated that fragments exceeding the acceptance threshold of 4" remained in one well. An extended dissolution was conducted, and reproving indicated that fragment levels were less than the acceptance threshold.

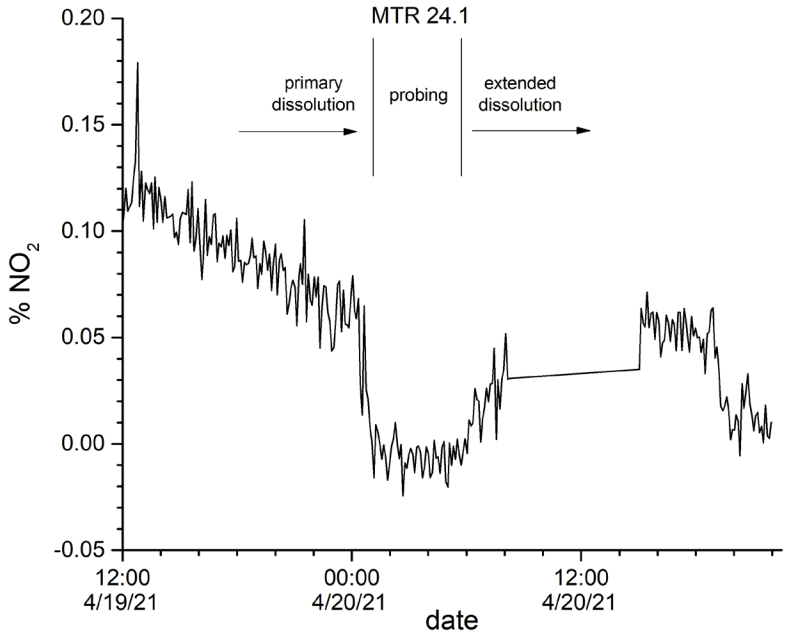

Figure 3-7. Evolution of %NO_2 during tail end of primary and extended dissolutions.

In Figure 3-7 it can be seen that the primary (incomplete) and extended (completed) dissolutions differ in the absolute NO_2 concentration and rate of change of that concentration. Also, the %NO_2 levels when the dissolver is heated and purged are higher than the values when the dissolver is off. These general observations are true to all of the monitored runs, regardless of the dissolver being monitored or the laser used to generate the Raman spectrum. It was further observed that there is a qualitative correlation between probe height measurements and properties of the %NO_2 measurements. Specifically, %NO_2 values tend to be higher, and the slope of the curve steeper, when the probe height value is larger.

The qualitative observations suggest that a more quantitative relationship between %NO_2 readings and probe height might be deduced. If this can be accomplished, it would be possible to use the Raman offgas monitor to estimate the fragment height in the dissolver in real time. This capability would allow the optimization of process operations with respect to the continuation of a dissolver run. The presence of excessive fragments could be detected without resorting to probing. Also, detection of the dissolution endpoint if it occurred before the prescribed dissolution time would save time and costs.

The only data available to establish the correlation between %NO_2 readings and probe height comes at the end of a run, with the last few measurements before the dissolver is cooled and the solution is probed. Both the process evolution profiles and laboratory flowsheet development studies indicate that the dissolution rate slows near the end of the run. It is reasonable to assume that the last several %NO_2 measurements in the run before the dissolver is cooled correspond to a similar fragment height. Inclusion of multiple measurements from a run helps compensate for the comparatively high measurement uncertainties of %NO_2 at trace levels.

The qualitative trends described above indicate that it is not only the instantaneous %NO_2 reading but also the rate of change of that reading that corresponds to fragment height. Thus, evaluation of the dissolver status should include, in addition to the most recent reading, a number of the immediately preceding readings. For this analysis, the relevant data set for a given time is assumed to be the twenty most recent

measurements. This set of readings is a "measurement window" that slides forward in time with each new instantaneous %NO_2 measurement. The potential correlations between readings and fragment height are evaluated via Partial Least-Squares (PLS) analysis. PLS does not rely on assumptions about underlying structure to the data, instead providing an empirical analysis.

PLS analysis for a single batch (HFIR Batch 11) demonstrates the possibilities of this approach. From this batch, the primary dissolution of the first run resulted in a fragment height that was in excess of 10" (the maximum quantifiable height detected by the probing dial). Therefore, this data was not included in the analysis. However, the extended dissolution for the first run and the second through fifth runs all concluded with fragment heights below 10". For each of these runs, a set of the last five windows of 20-point %NO_2 readings was collected and assigned a fragment height equal to the probe reading. Probe heights in this set ranged from 0" to 7.5", all within the 8" acceptance limit for HFIR.

The ability of the model to replicate the input data is shown in Figure 3-8. The runs within the batch were self-consistent, with a standard error of prediction for the fragment height of ~2.5" using a model with one principal component (shown in the inset). This prediction error for the input data seems reasonable considering the limitations and assumptions made in generating this data, including that the last five measurement windows all correlate to the same fragment height, any potential uncertainty in reading the probe indicator dial, and the limitation that the probe measurement only being sensitive to the highest height in either well, not indicating the fragment level in the other well. As will be discussed below, further analysis is needed to address the limitations and assumptions noted here.

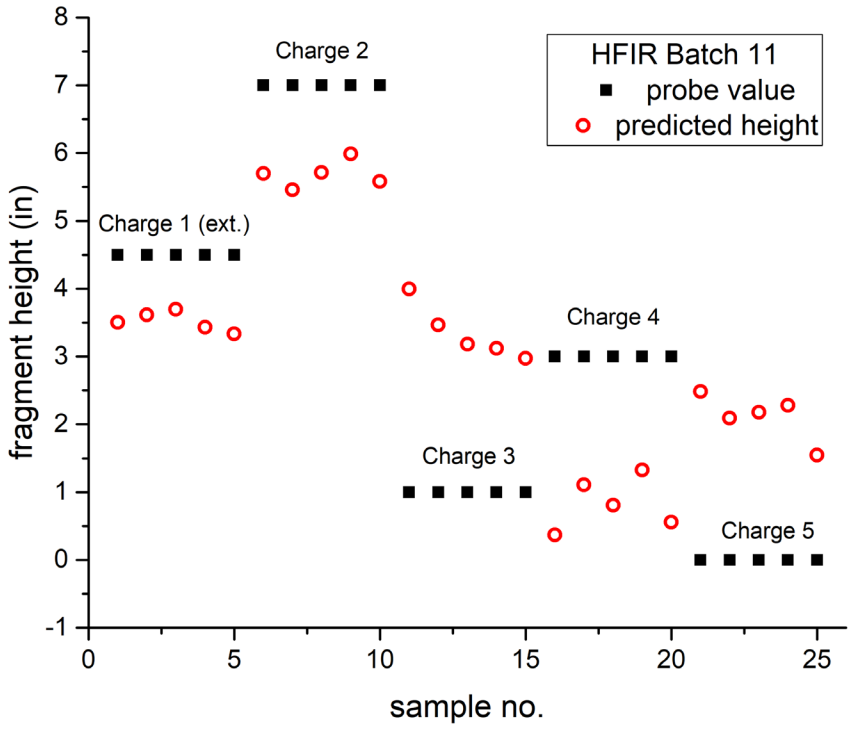

Figure 3-8. PLS model predictions for fragment height, HFIR Batch 11.

The model can be used to interpret the % NO_2 readings earlier in the evolutions for the five charges, to assess when fragment heights may have gone below the acceptable 8" limit. These measurements are shown in Figure 3-9. Fragment height predictions greater than 8" are shown in black, and those less than 8" are shown in green.

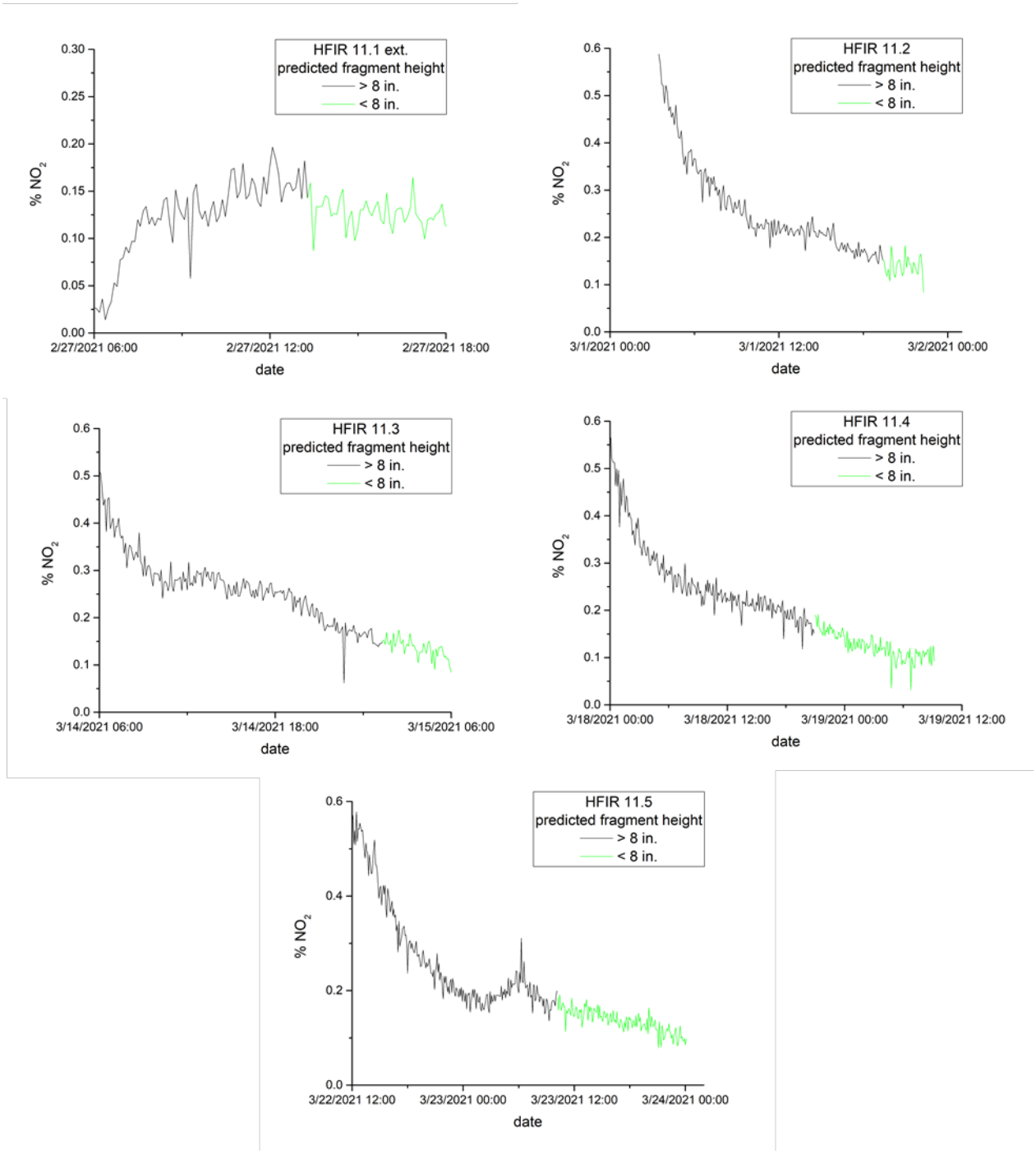

Figure 3-9. Predicted transitions below fragment height limits for HFIR Batch 11.

The PLS predictions can also be used to estimate a rough rate of fragment height decrease during the tail of the dissolution for each run. This information could provide an estimate of the time at which a processing run might be expected to be done once the PLS prediction indicates that the 8" threshold fragment level has been reached. Ideally, this calculation would be performed individually for each charge using data obtained from multiple batches. This approach would account for the slower processing rates associated with the

later charges in a batch. Until that data is obtained, a less precise estimate can be found through the average rate of decline across all five charges. For each charge in Batch 11, the rate is calculated by choosing as the starting point the measurement when the fragment height is predicted to be below 8", as the ending point the last measurement, and dividing the predicted change in height by the elapsed time. The average rate was observed to be 0.9 (± 0.2) inches/hour.

A similar analysis applying the PLS methodology to the data obtained in the three runs monitored in HFIR Batch 13 reproduces the observations in that batch with a similar degree of accuracy. This type of analysis seems to be feasible for the analysis of charges in a given batch, being applied retroactively to determine what happened. A more useful PLS model, however, will need to be accurate across multiple batches and be predictive in real time. Additional data and analysis are required to achieve this level of performance. For example, the Batch 11 and Batch 13 data are not consistent. Using the Batch 11 data to predict Batch 13 measurements, and vice versa, does not yield satisfactory results. Combining the Batch 11 and Batch 13 data into one set also does not yield a consistent prediction. This inconsistency is attributed primarily to the use of a different excitation laser – or more specifically the different $\%NO_2$ calibration associated with each excitation wavelength. At the trace levels present, small relative offsets of the two calibrations will be significant. To confirm this hypothesis, the results from future processing runs can be compared to the appropriate data set (532 nm excitation with Batch 13, or 640 nm excitation with Batch 11). This analysis also does not account for any small differences in sparge or purge rates, operating temperature, or the current acidity or aluminum or uranium concentration in the dissolver. It also does not consider which charge is being dissolved within the batch sequence. These process conditions can have small effects on the dilution of NO_2 within the offgas and on the rate of dissolution for a given amount of material remaining in the dissolver. Further study is required to understand which of these factors significantly affects the accuracy of the PLS dissolution model.

In principle, $\%NO_2$ readings from the MTR runs can also be analyzed this way. Unfortunately, there are several reasons why this cannot be done with the data obtained from the batches analyzed herein. Fragment heights were only recorded as "less than 4 inches" if they passed the acceptance threshold. This practice prevents any investigation of the quantitative relationship between $\%NO_2$ reading and fragment height. Also, the Batch 22 and 24 runs were conducted with a leak in the dissolver lid. As can be seen in the elution profiles in Appendix A, peak $\%NO_2$ rates and the shape of the elution profiles were inconsistent between runs, suggesting that the quality of the lid seal changed with each charge. The analyses from these runs could not be compared with the one (leak-free) measurement obtained from Batch 26. Additionally, the change to the (6,6) charging scheme for Batch 26 could result in a different dissolving rate compared to the (3,4,5) scheme of the previous runs. Monitoring and probing results for future runs could be compared to Batch 26 data to try to create a consistent fragment height prediction model.

3.3.3 Reducing process time with real time monitoring

As described in Section 1.3, an accurate assessment of the remaining fragments in a dissolver can lead to improved processing efficiencies. This happens when high probe readings are averted and when the dissolver is not run after the material is fully dissolved.

The cost avoidances associated with the high probe scenario are summarized in Table 3-4. The time lost due to a high probe assumes a sequence of events where the dissolver is cooled and probed as usual per procedure. Upon discovery of the high fragment level, the dissolver is closed and reheated, with the extended dissolution proceeding for a prescribed period depending on the dissolver. Finally, the dissolver is cooled and probed again. The replacement scenario assumes that instead, the dissolver is operated for 6 hours beyond the point when the threshold fragment level is indicated by the monitor, with subsequent cooling and probing per procedure. The 6-hour assumption accounts for the uncertainty of the fragment height estimate by allowing for additional dissolving. As the model is refined based on additional data, the

extension may become shorter. Nonetheless, the template for estimating the time avoidance would remain the same.

For the HFIR Batch 11, Charge 1 run, there was an excess of fragments detected after the primary dissolution (probed > 10" per the procedure). When the PLS model for Batch 11 was applied to the $\%NO_2$ readings for the primary dissolution, the estimated fragment height at the end of dissolution was found to be between 8 – 8.5". The maximum estimated height shown during the extended dissolution was also between 8 – 8.5" after the dissolver fully heated and fragment dissolution resumed its full rate. At that point, dissolution was continued for 4 hours, with a decrease of ~4.5" in estimated fragment height. These observations support the use of the 6-hour estimate for prolonged dissolution in the high probe cost avoidance estimate and indicate that implementation of this scheme may have avoided the high probe in this instance.

Table 3-4. High probe cost avoidance calculation.

	Activity	HFIR	MTR	Comments
Time lost in high probe (hours)	Cool the dissolver	2	2	
	Probe	2	2	
	Heat and extend dissolution	25	14	Estimated by H-Canyon Engineering
	Cool the dissolver	2	2	
	Probe	2	2	
	Total	**33**	**22**	
Time committed to avoid high probe (hours)	Extend the primary dissolution	6	6	See text
	Cool the dissolver	2	2	
	Probe	2	2	
	Total	**10**	**10**	
Net savings per high probe (hours)		**23**	**12**	
Average no. high probes per batch		1	0.25	Assumption based on recent averages
Number of batches per year		9	18	Intended processing schedule
Detection accuracy		0.95	0.95	Assumed, taking credit for conservatism associated with the extra 6 hours of dissolution
Estimated cost avoidance per year (hours)		**197**	**51**	

Another means by which input from the offgas analyzer might be used to reduce process time is by facilitating accelerated charging of new material into the dissolver. In this approach, for all charges except the last charge in a batch, the dissolver would be stopped as soon as possible after reaching the fragment height fell below the threshold limit. New material would be added to dissolver on top of whatever fragments existed. The time chosen to do this would be based on the observation of a particular $\%NO_2$ level in the offgas, with sufficient conservatism to reflect the uncertainty of the correlation between $\%NO_2$ reading and fragment height.

The justification for considering accelerated charging rests on the fact that the current dissolution procedure already allows charging with some material present. For MTR, in the scheme with 2 charges of 6 bundles each, a 36" fragment height is allowed after the first dissolution. For HFIR, after dissolutions 1-4, an 8" fragment height is allowed. These heights are permitted based on criticality concerns, hydrogen concerns, and/or the ability to physically close the dissolver lid after charging.

The fragment height estimates for HFIR Batch 11 in Figure 3-9 show that for Charges 2-4, dissolution was stopped approximately 3, 4, and 12 hours, respectively, after the estimated fragment height reached 8". (Charge 5 needed to go further to completion per procedure, and Charge 1 needed an extended dissolution.) If the 6-hour extension proposed in the high probe avoidance scenario were applied to these runs, Charges

2 and 3 would have run longer and Charge 4 would have been shorter. These findings suggest that a more precise model to estimate fragment height will likely be required to realize cost savings associated with accelerated charging for HFIR runs.

For MTR runs, the opportunity to gain time through accelerated charging is limited by the transition to the (6,6) charging scheme. There is only the transition from the first to the second change that could be shortened with the charging. On the other hand, the probing results shown in Table 3-1 indicate that the fragment height threshold used for these runs was 4", not 36". This large difference suggests that even with a single opportunity of accelerated charging, substantial time savings could be realized. The acquisition of additional data to support the $\%NO_2$ / fragment height correlation in MTR dissolver runs is warranted.

3.3.4 NO_2 signal integration

The time trace of $\%NO_2$ readings for a given charge can be integrated to show the progress of the dissolution towards completion. The integrations of separate charges can be compared to discover or confirm trends in dissolver operation. To make these comparisons, several assumptions are necessary.

- The start and end times for the integration are estimated from the $\%NO_2$ profile.
- The start time is determined from the rise of $\%NO_2$ from the baseline levels measured prior to the dissolution of the material.
- For HFIR runs,
    - If the dissolver has been allowed to run to completion (as indicated by 0" fragment height being detected with probing), the end time is assumed to be the time when the dissolver is turned off. No attempt is made to determine if the fragment height may have reached 0" prior to shutdown. Completion times may be overestimated for these runs.
    - If probing indicated that 1-8" of fragments remained, the time required to reach 0" fragment height and the extrapolated shape of the $\%NO_2$ curve during that time must be estimated. This estimate is generated with a simple exponential fit of the $\%NO_2$ near the end of the run, and extrapolation based on the average tail end rate of 0.9"/hour described in Section 3.3.2.
    - For Batch 11, Charge 1, where an extended dissolution was required, the $\%NO_2$ profile for the extended dissolution is grafted onto the primary dissolution to simulate a continuous process. The extended dissolution is grafted from the point where the $\%NO_2$ profile best matches the profile at the end of the primary dissolution.
    - Both the extrapolation and grafting approaches are likely to result in an uncertainty of several hours for the total dissolution.
- For MTR runs,
    - If the fragment height was determined to be less than 4", the run is assumed to have gone to completion when the dissolver was stopped. This will introduce an uncertainty, possibly of several hours, in the estimates of completion time.
    - For both Batch 24, Charges 1 and 3, a 5" fragment height was observed after the primary dissolution was completed. For these runs, the data from the extended dissolution was appended to the primary dissolution to simulate a single, continuous run.
    - For Batch 22, integrations are only calculated for Charge 3. For Charge 2, the peak $\%NO_2$ level is depressed by a factor of 3-4x compared to other runs, presumably due to dilution of the offgas associated with air leaks in the dissolver lid. If this dilution factor pertains to the end of the run, the $\%NO_2$ level will be at or below the LOD and the integration will not capture the full amount of material released. For Charge 1, the Raman data is incomplete due an extended instrument malfunction. Also, for Charge 3, the run was stopped partway through the prescribed time due to low liquid levels in the dissolver and restarted after the

liquid level was topped off. The $\%NO_2$ profiles for the two parts are joined and treated as one run.

- Any NO_2 present is produced from material dissolution. There is some amount of NO_2 that dissolves in nitric acid and will not be measured. It is assumed, for the purposes of this comparison, that the liquid is saturated with NO_2 gas very early in the dissolution and the amount needed for saturation is negligible compared to the total amount of NO_2 released during the dissolution.
- Each charge will be internally normalized so that the integration runs from 0-100%. This step corrects for any issues associated with dissolver leaks (MTR Batches 22 and 24) and eliminates any differences associated with different amounts of material in each charge.

Appendix B shows the integrated, normalized profiles for the 13 runs. Observations of interest include:

- For MTR Batch 22, Charge 3, at the conclusion of the initial dissolution slightly more than halfway through the prescribed duration, 96.4% of the total NO_2 had been generated. The final 26 hours generated only 3.6% of the total. As noted in Table 3-1, probing after the initial period showed one well with a fragment height of 24" and the other three wells at 4". Given that the initial bundle length was 132" (11.5'), and thus 132" x 5 = 660" of material was initially charged, then at least (660-24-(5x4))/660 = 93.9% of the material was dissolved when the run was stopped. (The actual completion is likely higher, considering that the fragment diameter was probably less than the initial value.).
- For MTR Batch 24, Charge 1, at the conclusion of the primary dissolution, 99.4% of the total integrated NO_2 signal had been accumulated. The 5" fragment height found in one well implies a total dissolution of (660-5)"/660" = ≥99.24%.
- For MTR Batch 24, Charge 3, at the conclusion of the primary dissolution, 98.3% of the total integrated NO_2 signal had been accumulated. The 5" fragment height found in one well implies a total dissolution of (660-5)"/660" = ≥99.24%.
- For HFIR Batches, the probing did not indicate if the fragments found were associated with the inner or outer HFIR element, and did not indicate the fragment height (if any) in the other well. Thus, it is not possible to estimate percent completion based on the fragment height observation. Estimates, based on $\%NO_2$ integrations, of percent completion at the end of runs with fragment heights are:
    - Batch 11, Charge 2: 98.3% (7.5" fragment height)
    - Batch 11, Charge 3: 99.7% (1" fragment height)
    - Batch 11, Charge 4: 99.2" (3" fragment height)
    - Batch 13, Charge 1: 97.1% (7.5" fragment height)
    - Batch 13, Charge 2: 96.3% (5" fragment height)

The general agreement between the integrated NO_2 signal and the measured fragment height suggests a correlation between the two measurements. The uncertainties inherent to both quantities limit the precision of the correlation.

The integrated $\%NO_2$ signals show that the majority of the offgas production occurs in the early parts of a charge. Dissolution of the remaining material becomes slower towards the end, more so for MTR than HFIR. The difference between the two fuels may arise from their shapes. HFIR fuel is fully submerged during the entire charge, while MTR fuel is gravity-fed into the well and some portions of the material only contact the solution towards the end of the run.

3.3.5 Material balance considerations

Ideally, the readings of the Raman offgas monitor, alone or in combination with other process operating data, could be interpreted to give a measure of the mass of fuel that has been dissolved. If the gas sampling

point was located in the dissolver headspace, this calculation could hypothetically be performed by quantitation of the products in Equations 1-4 – particularly nitrogen-containing species. Percent values of these gases could be converted to absolute values by application of the air sparge and purge rates, assuming that the system is leak-free. Although the amount of nitric acid consumed to create both aluminum and uranyl nitrate is dependent on the solution acidity, this information is encoded in the instantaneous ratios of the product gases.

In practice, with the sampling point located downstream of the condenser and the silver nitrate reactor, any reactions associated with those elements must be considered. It was confirmed that additional reactions occur during peak dissolution periods due to the observations of O_2 deficit and N_2 surplus relative to concentrations in air. Any conversion would likely require use of these values in addition to the NO_2 measurements. Candidate reactions are described in some detail in Section 1.2. Despite that list, there are several unknowns that prevent a quantitative conversion of measured gases into mass of fuel dissolved.

Equations (5) and (6), which represent the conversion of NO to HNO_3, strongly favor the conversion to acid. However, it is not likely that all the HNO_3 is returned to the dissolver. Analysis of the liquid captured in the condensing trap located on the analytical trailer sample inlet line showed the solution to be strongly acidic and to have a dark brown color. Thus, there is an appreciable but unknown fraction of NO_x that does not reach the analyzer.

N_2O is apparently destroyed before reaching the analyzer, but the specific reactions associated with that process are not known. Temperatures in the offgas line do not reach the values required for spontaneous decomposition of N_2O, nor do they match the temperatures reported in the literature at which a catalyzed decomposition or reaction with NO could occur.[15] In a prior study at SRS, the analysis of numerous grab samples of stack effluent gas from the dissolution of aluminum-clad uranium slugs in F-Canyon also showed substantially more NO_2 than N_2O (70-120x during peak NO_2 emission).[28] However, this process removed most of the aluminum cladding with a 50-50% $NaNO_3$-NaOH solution before nitric acid attack. Thus, much of the current source for N_2O was not present in this historical example, and the results are not directly comparable (even assuming that the gas treatment was identical, which might not be the case). Recent studies in SRNL[29] examining the role that the silver nitrate-coated berl saddles may have in catalytic destruction of these species did not show any changes in the concentrations of N_2O and NO. The reason for the loss of N_2O remains unexplained.

Both considerations would influence the interpretation of the nitrogen balance in the basic dissolution equation (Equation 1). The acidity of the dissolvent determines the molar ratio of N_2O, NO, and N_2 formed in the dissolver headspace as well as the molar ratio of the sum of these gases to the 3 moles of N required to convert one mole of Al to $Al(NO_3)_3$. And, if the conversion pathway of N_2O is not known, it is uncertain whether it should be accounted for as NO_2 or N_2/O_2 growth.

The studies on silver nitrate-coated berl saddles show that under laboratory conditions consistent with process parameters, H_2 was catalytically recombined with O_2 with high efficiency (>97% for residence times of >10 s). As noted earlier, $\%O_2$ levels are depressed during NO_2 offgas to a greater extent that would be expected due to displacement. Loss of O_2 through recombination with H_2 as shown in the studies of the silver nitrate-coated berl saddles is one explanation for this observation. However, the loss of O_2 is not a quantitative proxy for loss of H_2, since O_2 is also lost during the recovery of nitric acid from NO in the condenser (see Eq. 5). Thus, uncertainties associated with this process hinder using O_2 loss as a means for working back to aluminum dissolution.

The potential accuracy of the estimate should also be considered. The accumulated uncertainties of the components in the calculation could exceed the precision required for the estimate to be meaningful. Uncertainties of N_2 and O_2 concentrations are 0.5% and 1.5% (1σ) of the reading, as described previously.

These uncertainties would be increased by 2 because the values of interest would be the excursion from the measurement baseline, obtained from the subtraction of two uncertain numbers. Based on the comparison of Raman intensities, the uncertainties of NO_2 readings during the peak of the dissolution will be somewhere between those of N_2 and O_2 – perhaps 1% (1σ) of the reading. The correction factor associated with the efficiency of the condenser will have an unknown uncertainty, perhaps on the order of several percent. The variation of the acidity of the dissolvent, and its effect on the ratio of species in the offgas, could contribute a few percent as well. Although not all these contributions to the uncertainty are quantifiable, it is reasonable to assume that they combine to an uncertainty of at least 5%.

One hypothetical example where the estimate of dissolved fuel would be of interest is as a confirmatory measurement that a large amount of material has not been dissolved (for example, something greater than the 36" fragment height threshold for MTR fuel remains in that dissolver). For a 6-bundle charge of fuel, with each bundle being 132" long, a single fragment would comprise 4.5% of the total amount of material charged. This difference is exceeded by the likely uncertainty derived above.

4.0 Conclusions

SRNL Sensing and Metrology and Advanced Engineering Divisions have developed an instrument based on Raman spectroscopy to monitor offgases associated with nuclear fuel dissolution in H-Canyon. The spectrometer is in an analytical trailer owned by SRNL outside the facility and samples offgases from the 6.1D or 6.4D dissolvers. The instrument is capable of simultaneously monitoring multiple gases that are characteristic of the aluminum dissolution process and tank purging, including N_2O, NO, NO_2, H_2, H_2O, N_2, and O_2. The instrument was used to monitor 15 charges across multiple batches for both the MTR and HFIR processing campaigns.

The only molecular species observed in the offgas stream of either dissolver were NO_2, H_2O, N_2, and O_2. The other species are presumed to have been oxidized or decomposed into the above species, although the chemistry of that conversion is not fully known. Nonetheless, the $\%NO_2$ composition of the offgas was found to be a qualitative indicator of the activity in the dissolver, with features of the time profile of the evolution correlating to process activities.

The analyzer is sensitive to the differences between NO_2 generated during the tail end of the dissolution and released by sparging the dissolvent. This sensitivity was observed with both 640 nm (pre-resonant) and 532 nm (resonant) excitation. An empirical correlation was developed to relate $\%NO_2$ readings to fragment height using probe measurements following dissolution runs. Correlations were established within individual batches but could not be transferred between batches. Examples were provided to show how a more precise and universal version of this correlation could be used to reduce the incidence of "high probes". Estimates of time savings due to the avoidance of this scenario were provided for both MTR and HFIR dissolution processes. A discussion of how these correlations could be used to support accelerated charging and realize further time savings was presented. There is currently too much uncertainty to support the use of the correlation in this manner, and additional work is needed.

Integrations of the $\%NO_2$ profile were presented for each dissolver run monitored. The general trends seen are consistent with expectations for the kinetics of the dissolver operation; for example, dissolver runs proceed more slowly with successive charges. The profile of the $\%NO_2$ evolution demonstrates that most of the material is dissolved in the initial 50-60% of each dissolution run. The possibility that the integrated $\%NO_2$ reading could be used to estimate the amount of material dissolved was considered; gaps

in the understanding of the chemistry of the offgas and uncertainties in the Raman measurements make this calculation currently intractable.

5.0 Recommendations, Path Forward or Future Work

The Raman offgas analyzer has provided useful information regarding endpoint detection for dissolving and an assessment of the degree to which the dissolving is completed. Due to changes in the Raman instrumentation (particularly the choice of excitation laser), occasional instrument malfunctions, and issues with dissolver system in-leakage, the data obtained did not support a fully realized means for predicting fragment heights. It is recommended that the system continue to be used to provide feedback on dissolver operations to facility engineers and operators and to obtain data to support more accurate and precise analyses. The monitoring system and its deployment can also be improved, in the following ways.

- Combining more refined probing results (especially if the probing height is below 4" for MTR processing) and process parameters such as sparge and purge rates with tail-end $\%NO_2$ measurements can result in a more robust endpoint detection and support accelerated charging of the dissolvers. Additional information can be obtained by stopping the dissolution early and probing the dissolver to determine fragment heights at higher $\%NO_2$ concentrations. This would be done when the $\%NO_2$ has declined from its peak to a level that is substantial but still occurs significantly earlier than the total dissolution time. A possible range of $\%NO_2$ values at which to make these measurements is 0.2 – 0.5%. This information would help with the creation of procedures that would maintain both operational and criticality safety.
- H-Canyon typically runs both the 6.1D and 6.4D dissolvers simultaneously. However, the input line for the analytical trailer (and the Raman analyzer therein) accepts only one gas stream at a time. If both dissolvers are meant to be monitored simultaneously, then two sampling points must be identified. If the location of these two points means that the Raman analyzer must be moved out of the analytical trailer, then a suitable location for the instrument must be found. The location should provide protection from the environment.
- Monitoring two points simultaneously implies the development of two Raman analyzers. An alternative approach that would allow the use of a single spectrometer to monitor both sampling points would involve the use of a dual fiber input system. The Raman scattering collected from the two gas cells would be projected onto the top and bottom halves of the detector array. This approach would require software development to aid in the collection of the appropriate subsets of the pixel array. If this approach is chosen, separate gas cells and fiber runs will be required, as would be the case if two instruments were used. It is also worth considering that the gas cells do not have any retroreflection optics to improve the excitation and collection efficiencies. A signal increase of up to 3.5x could be expected with the implementation of these optics.
- Currently, there is no interface between the instrument and facility control system. SRNL personnel must visit the instrument periodically to download data, confirm and interpret results, and provide information to engineers and operators. This process usually occurs after a charge is completed. With the creation and continued improvement of methods for real-time interpretation of the results, SRNL and H-Canyon should determine a way to communicate readings automatically to the H-Canyon Control Room.
- This interface would also allow SRNL and H-Canyon personnel to know that the instrument is working properly.
- Relatedly, while the instrument control program has been improved since the initial deployment, it can be made more reliable.
- The results indicate that both 640 and 532 nm laser excitation is suitable for monitoring $\%NO_2$ at the sensitivity and speed required to make processing decisions. Use of 640 nm excitation is the preferred option, due to the spectral interferences between the resonance Raman and fluorescence lines from NO_2 and lines from other gas species that occur with 532 nm excitation.

6.0 References

1. E. Saldivar and H. Watson, *Savannah River Accelerated Basin Deinventory*, SRNS-RP-2019-00651, Rev. 0, Savannah River Site, Aiken, SC. 2019.
2. *Dissolver Probing Improvement Technology Maturation Plan*, SRNL-TR-2019-00312, Savannah River National Laboratory, Aiken, SC, October 2019.
3. R.J. Lascola, A. Judy, and P.E. O'Rourke, *Feasibility Study of Using a LiDAR Sensor for Fuel Dissolution Monitoring*, SRNL-STI-2020-00412, Savannah River National Laboratory, Aiken, SC, October 2020.
4. T.S. Rudisill, W.E. Daniel, and P.E. O'Rourke, *Dissolution of Material Test Reactor Fuel in an H-Canyon Dissolver*, SRNL-STI-2016-00725, Rev. 1, Savannah River National Laboratory, Aiken, SC, May 2018.
5. T.S. Rudisill, W.E. Daniel, P.E. O'Rourke, *Evaluation of Changes to the MTR Fuel Dissolution Flowsheet to Increase the Number of L-Bundles Charged to a Dissolver"*, SRNL-STI-2020-00145, Savannah River National Laboratory, Aiken, SC, May 2020.
6. T.T. Truong, *Status Report on FCA Plate Electrolytic Dissolution Studies*, SRNL-STI-2019-00620, Rev. 1, Savannah River National Laboratory, Aiken, SC, December 2019.
7. H.M. Felmy *et al.*, *On-Line Monitoring of Gas-Phase Molecular Iodine Using Raman and Fluorescence Spectroscopy Paired with Chemometric Analysis*, Environmental Science & Technology, **10.1021/acs.est.0c06137** (2021).
8. M.P. Buric, J. Falk, S. Woodruff, B. Chorpening, *Gas Phase Raman Scattering: Methods and Applications in the Energy Industry.* In: Encyclopedia of Spectroscopy and Spectrometry (3rd Ed.), Volume 2, p. 8-17 (2017).
9. M. Aker *et al.*, Quantitative Long-Term Monitoring of the Circulating Gases in the KATRIN Experiment Using Raman Spectroscopy, Sensors, **20,** 4827 (2020).
10. M.L. Hyder *et al.*, *Processing of Irradiated, Enriched Uranium Fuels at the Savannah River Plant*, Report DP-1500, Savannah River Laboratory, Aiken, SC, April 1979.
11. R.G. Wymer and R.E. Blanco, *Uranium-Aluminum Alloy Dissolution*, Ind. Eng.Chem., **49**, 59-61 (1957).
12. R.W. Rice and D.V. Sarode, *Mercury-Catalyzed Dissolution of Aluminum in Nitric Acid*, Ind. Eng. Chem. Res., **40**, 1872-1878 (2001).
13. P. Marc, A. Magnaldo, A. Vaudano, T. Delahaye, and E. Schaer, *Dissolution of Uranium Dioxide in Nitric Acid Media: What Do We Know?"*, EPJ Nuclear Sci. Technol., **3**, 1-13 (2017).
14. *Compilation of Air Pollutant Emissions Factors (AP-42)*, U.S. Environmental Protection Agency, Chapter 8: Inorganic Chemical Industry. https://www.epa.gov/air-emissions-factors-and-quantification/ap-42-compilation-air-emissions-factors.
15. M.C.E. Groves and A. Sasonow, *Uhde EnviNO_x(R) Technology for NO_x and N_2O Abatement: A Contribution to Reducing Rmissions from Nitric Acid Plants*, J. Integrative Env. Sci., **7**, 211-222 (2010).
16. S.P. Tan and M. Piri, *Modeling the Solubility of Nitrogen Dioxide in Water Using Perturbed-Chain Statistical Associating Fluid Theory*, Ind. Eng. Chem. Res., **52**, 16032-16043 (2013).
17. J.B. Lefers and P.J. van den Berg, *Absorption of NO_2/N_2O_4 into Diluted and Concentrated Nitric Acid*, The Chemical Eng. J., **23**, 211-221 (1982).
18. W.E. Daniel, T.S. Rudisill, and P.E. O'Rourke, *Dissolution of Material Test Reactor Fuel in an H-Canyon Dissolver*, SRNL-STI-2016-00725, Rev. 1, Savannah River National Laboratory, May 2018.
19. W.E. Daniel, T.S. Rudisill, P.E. O'Rourke, and N.S. Karay, *Dissolution Flowsheet for High Flux Isotope Reactor Fuel*, SRNL-STI-2016-00485, Rev. 1, Savannah River National Laboratory, December 2017.
20. W.E. Daniel, T.S. Rudisill, and J.I. Mickalonis, *Evaluation of the Dissolution Behavior of L-Bundle End Caps and HFIR Fuel Carriers*, SRNL-STI-2019-00146, Savannah River National Laboratory, July 2020.
21. H. Keller-Rudek, G.K. Moortgat, R. Sander, and R. Sörenson, *The MPI-Mainz UV/VIS Spectral Atlas of Gaseous Molecules of Atmospheric Interest*, Earth Syst. Sci. Data, **5**, 365-373 (2013).
22. A.C. Vandaele *et al.*, *High-resolution Fourier Transform Measurement of the NO_2 Visible and Near-infrared Absorption Cross-section: Temperature and Pressure Effects*, J. Geophys. Res., **107(D18)**, ACH 3-1 – ACH 3-12 (2002).
23. H.D. Bist, J.C.D. Brand, and R. Vasudev, *The Resonance Raman Spectrum of Nitrogen Dioxide*, J. Mol. Spectrosc. **66**, 399-410 (1977).
24. W.F. Pearman, J.C. Carter, S.M. Angel, and J.W.-J. Chan, *Multipass Capillary Cell for Enhanced Raman Measurements of Gases*, Appl. Spectrosc., **62**, 285-289 (2008).
25. C. Wen, X. Huang, C. Shen, *Multiple-pass Enhanced Raman Spectroscopy for Fast Industrial Trace Gas Detection and Process Control*. J Raman Spectrosc., **51**, 781–787 (2020).

26. ASTM E1840-96(2014), *Standard Guide for Raman Shift Standards for Spectrometer Calibration*, ASTM International, West Conshohocken, PA, 2014, www.astm.org.
27. P.E. O'Rourke, *Calibration of Raman Spectrometer for Gas Phase Measurements*, SRNL-STI-2020-00202, Savannah River National Laboratory, May 2020.
28. E. Villa, *Analysis of F-Canyon Effluents During the Dissolution Cycle with a Fourier Transform Infrared Spectrometer/Multipath Cell*, WSRC-TR-97-0087, Savannah River Technology Center, 1997.
29. K. Taylor-Pashow, *Recombination of Hydrogen in the Iodine Reactors*, SRNL-STI-2021-00483, Savannah River National Laboratory, November 2021.

Appendix A. Process Runs

The following observations were made for gases evolved during the 15 H-Canyon dissolutions observed. Results for % NO_2, % N_2, and % O_2 are normalized to the sum of those three values. Thin lines indicate periods when the analyzer was not working. Other mid-run process or analyzer anomalies are noted on the figure.

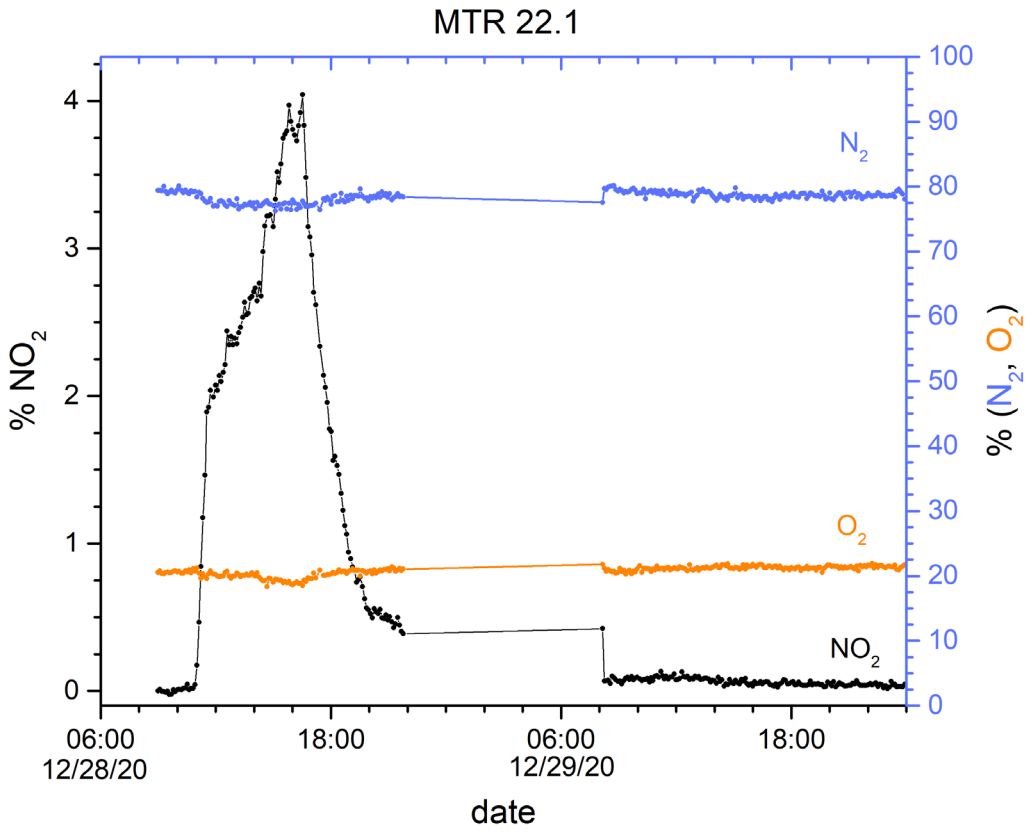

Figure A-1. Offgas evolution, MTR Batch 22, Charge 1.

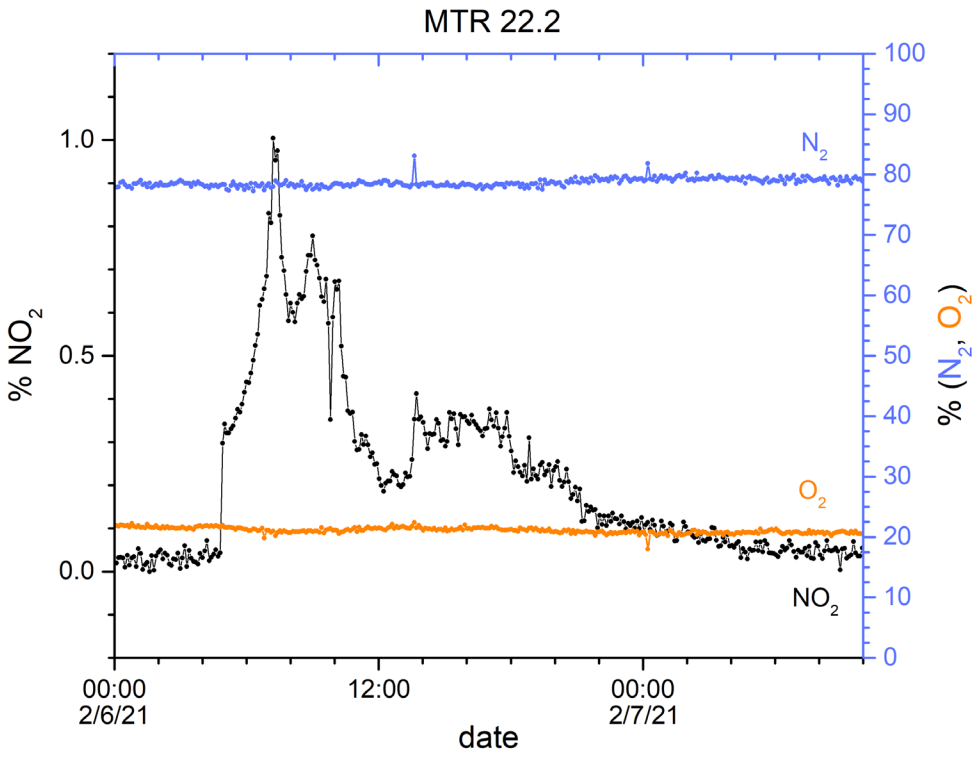

Figure A-2. Offgas evolution, MTR Batch 22, Charge 2.

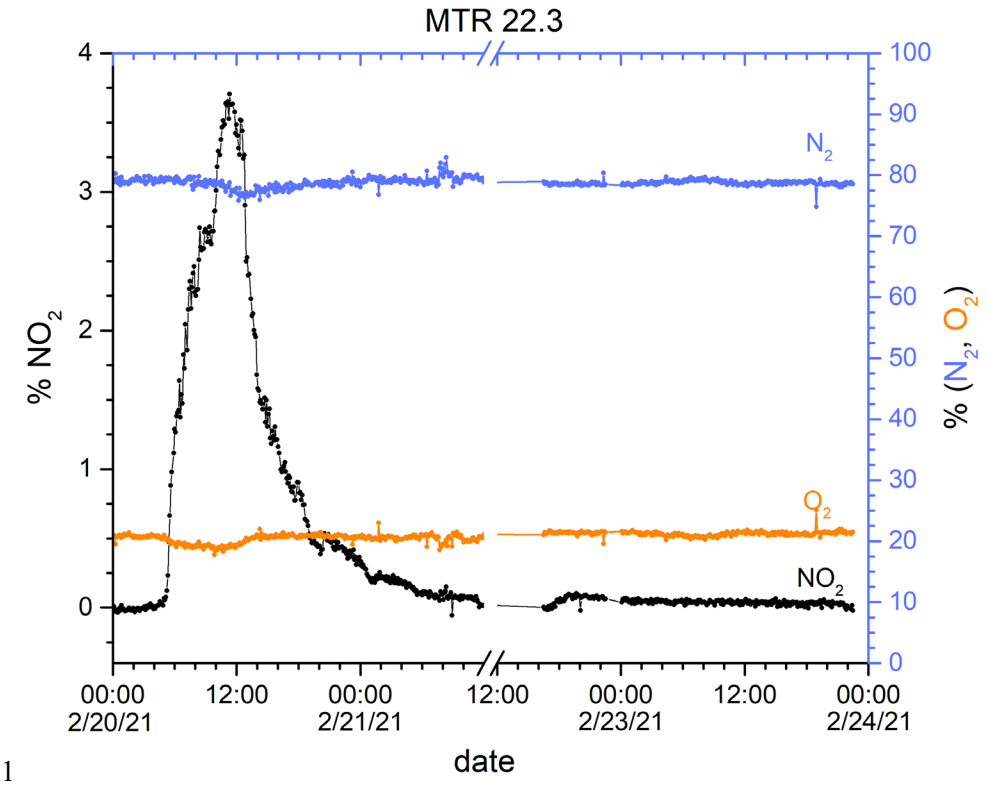

1

Figure A-3. Offgas evolution, MTR Batch 22, Charge 3

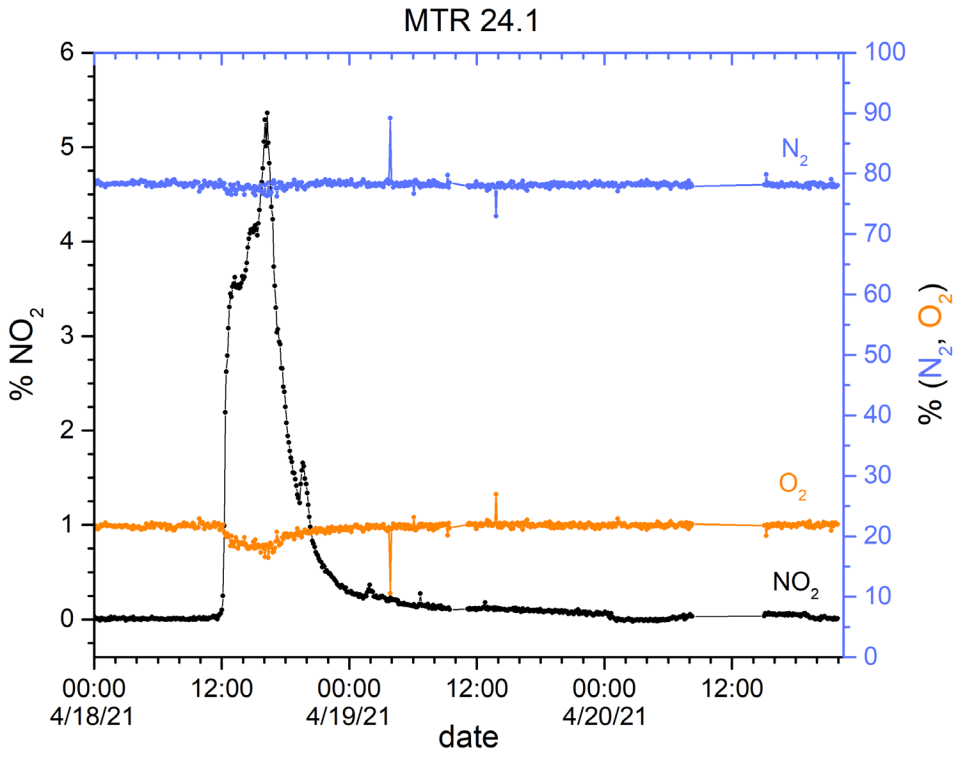

Figure A-4. Offgas evolution, MTR Batch 24, Charge 1.

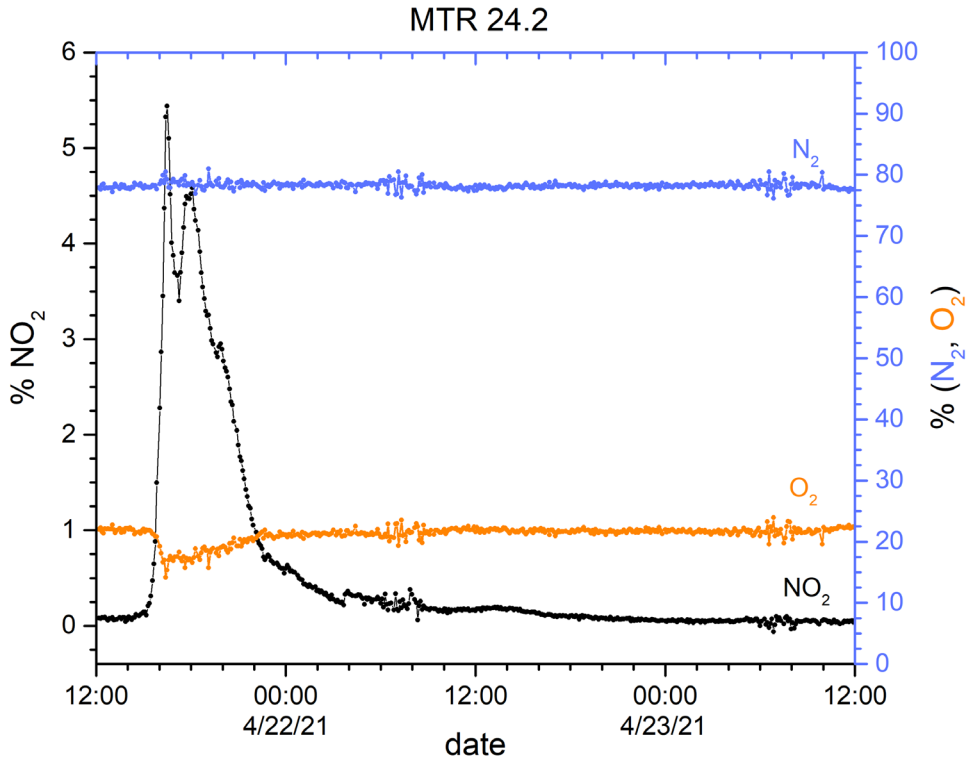

Figure A-5. Offgas evolution, MTR Batch 24, Charge 2.

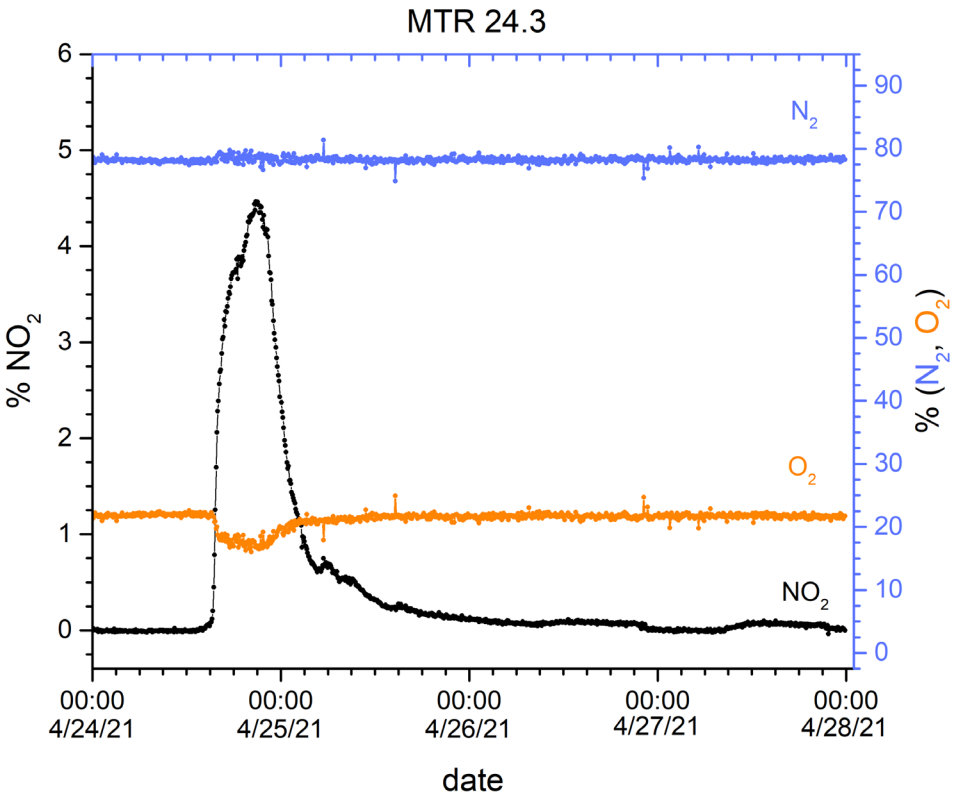

Figure A-6. Offgas evolution, MTR Batch 24, Charge 3.

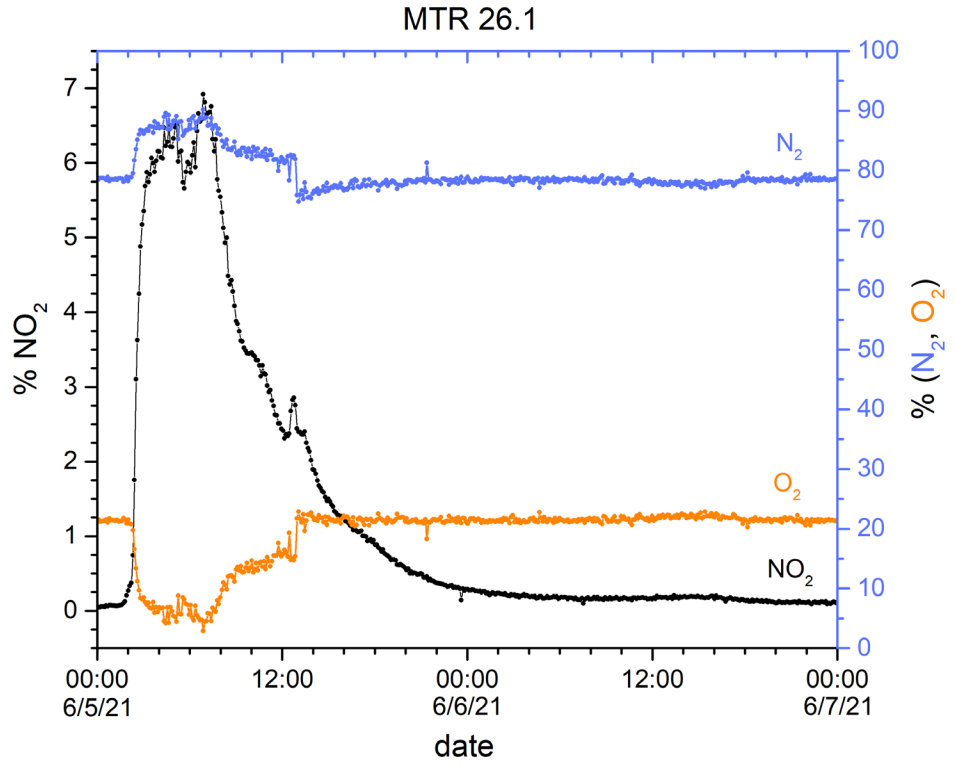

Figure A-7. Offgas evolution, MTR Batch 26, Charge 1.

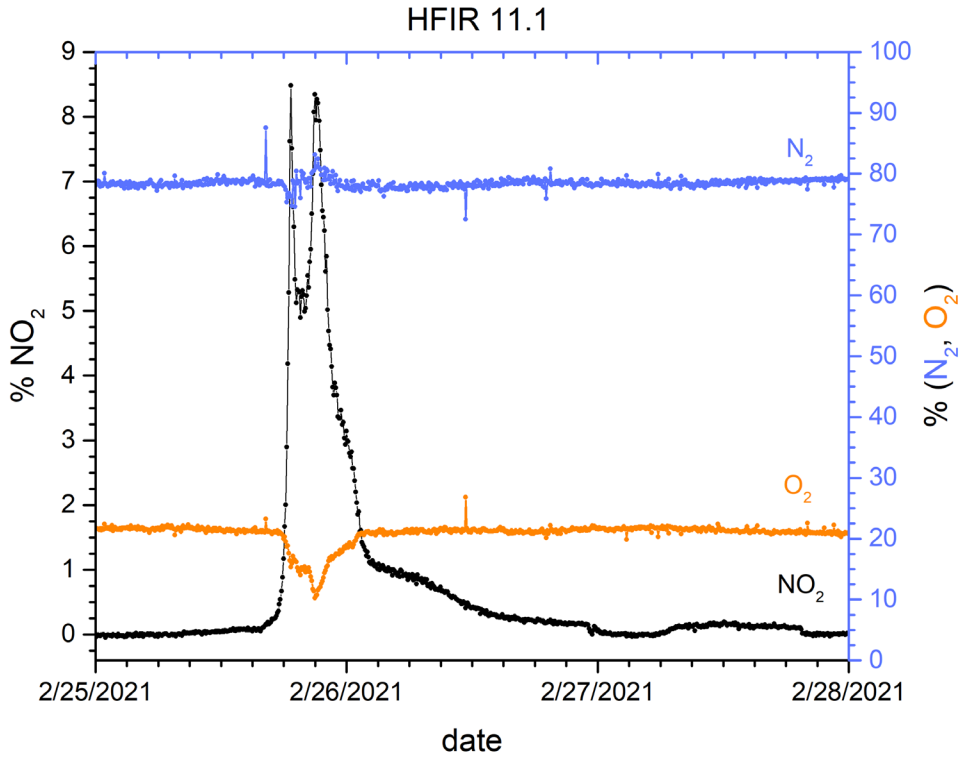

Figure A-8. Offgas evolution, HFIR Batch 11, Charge 1.

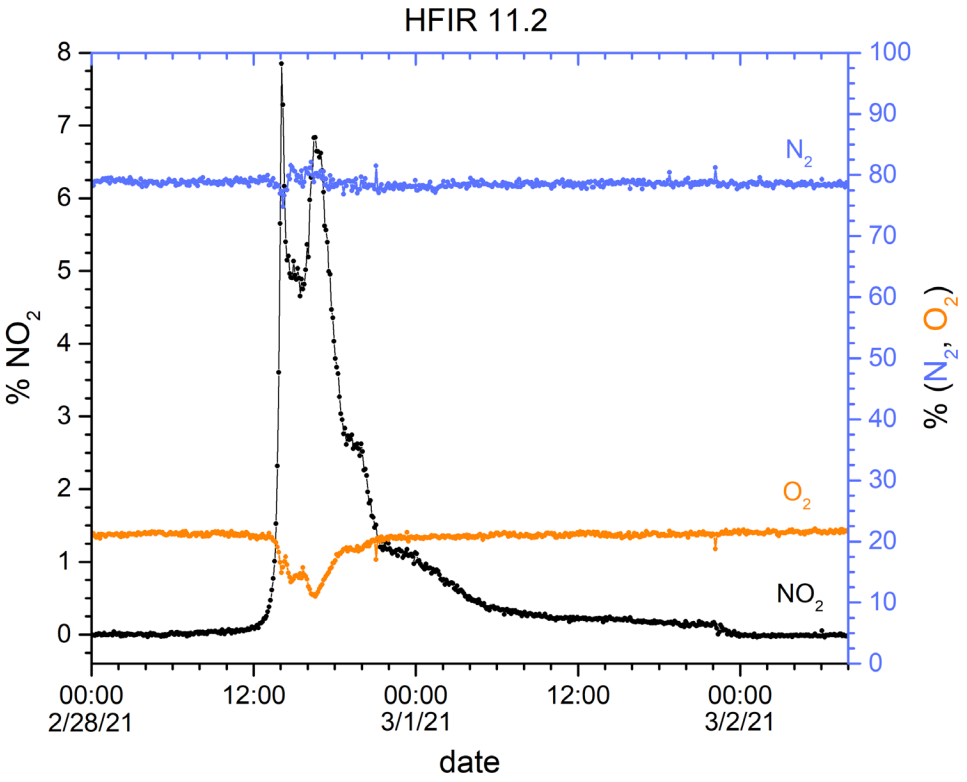

Figure A-9. Offgas evolution, HFIR Batch 11, Charge 2.

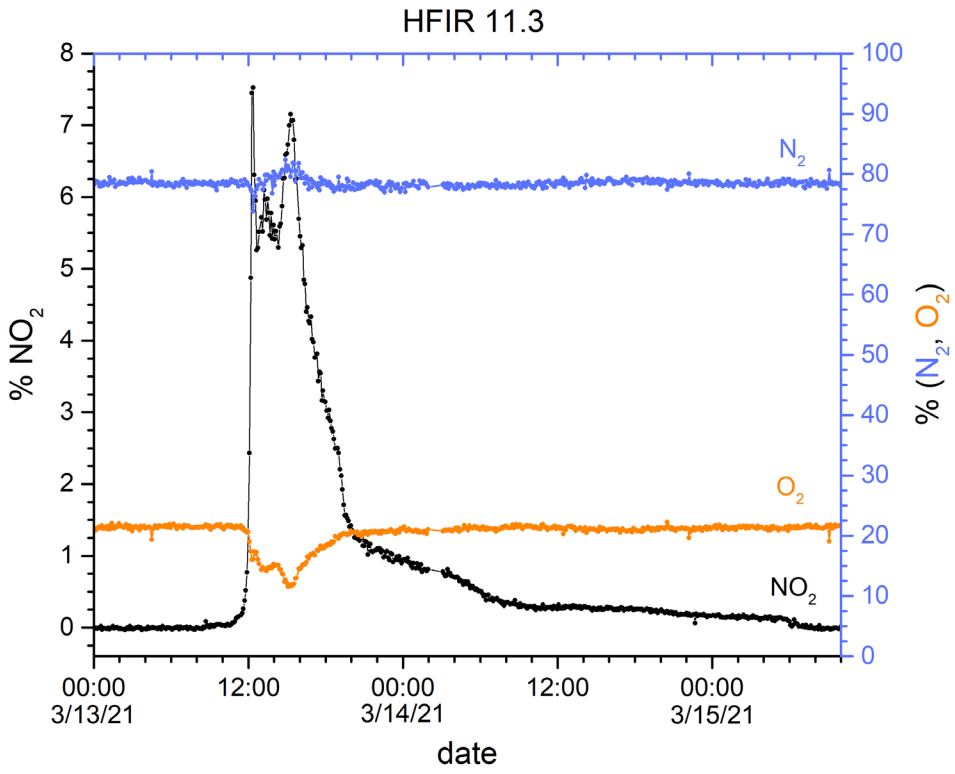

Figure A-10. Offgas evolution, HFIR Batch 11, Charge 3.

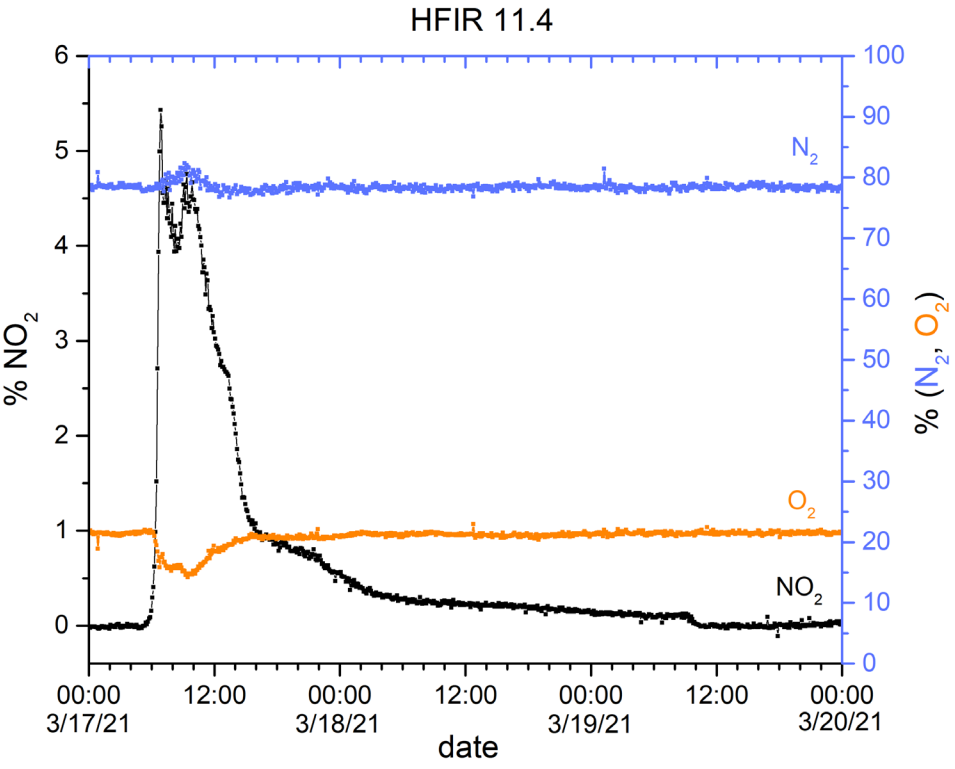

Figure A-11. Offgas evolution, HFIR Batch 11, Charge 4.

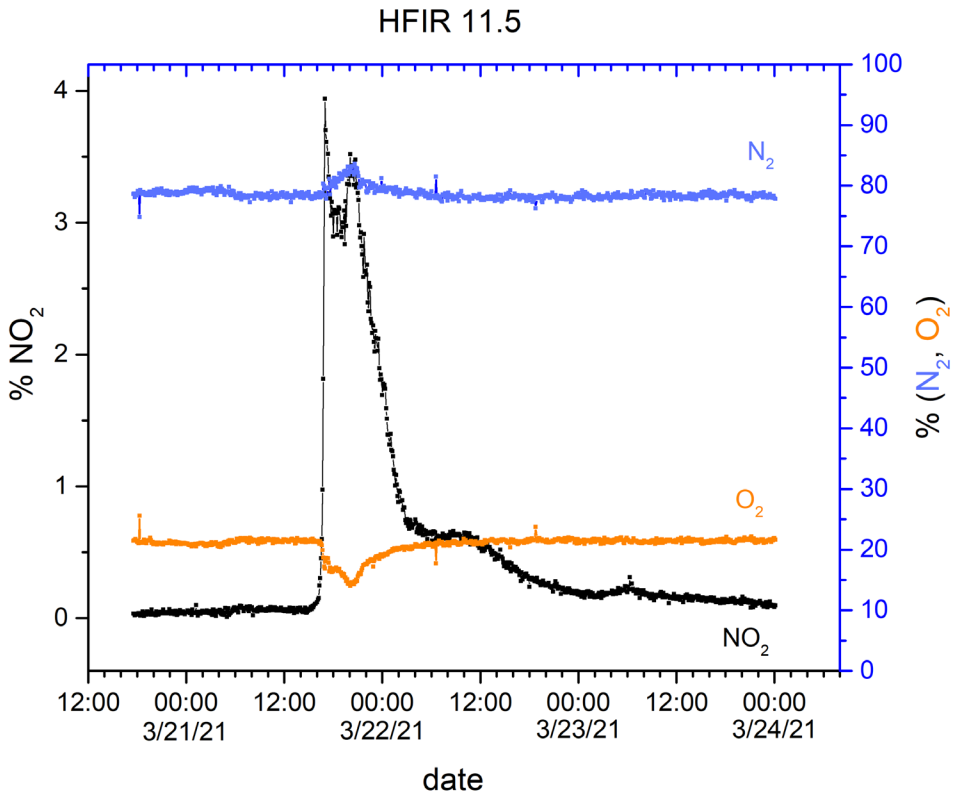

Figure A-12. Offgas evolution, HFIR Batch 11, Charge 5.

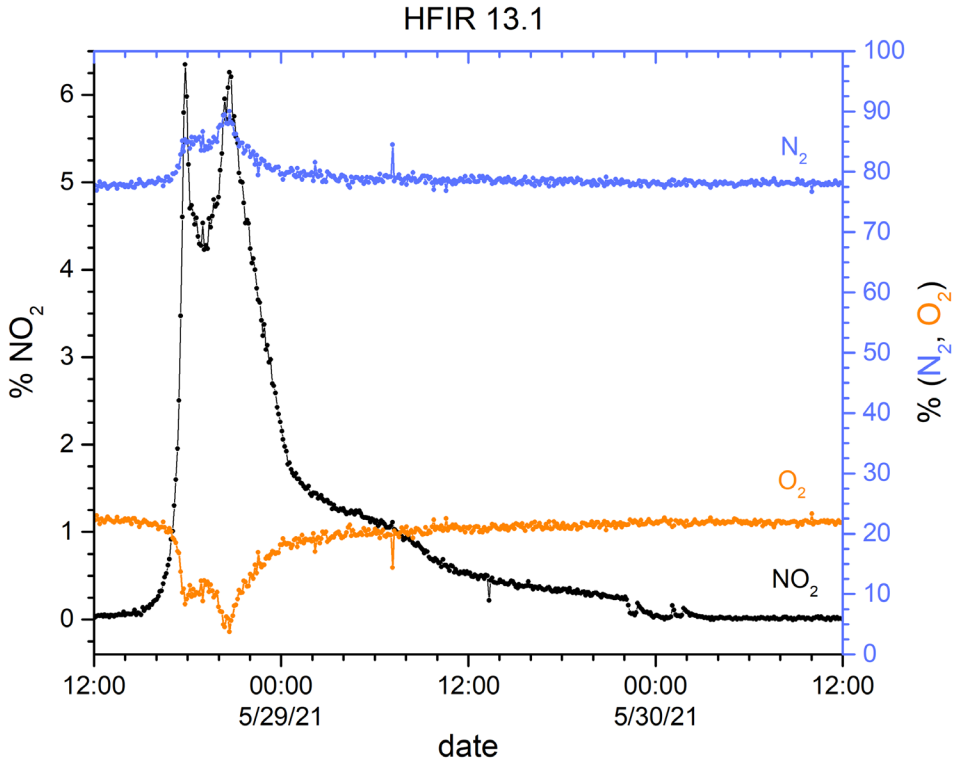

Figure A-13. Offgas evolution, HFIR Batch 13, Charge 1.

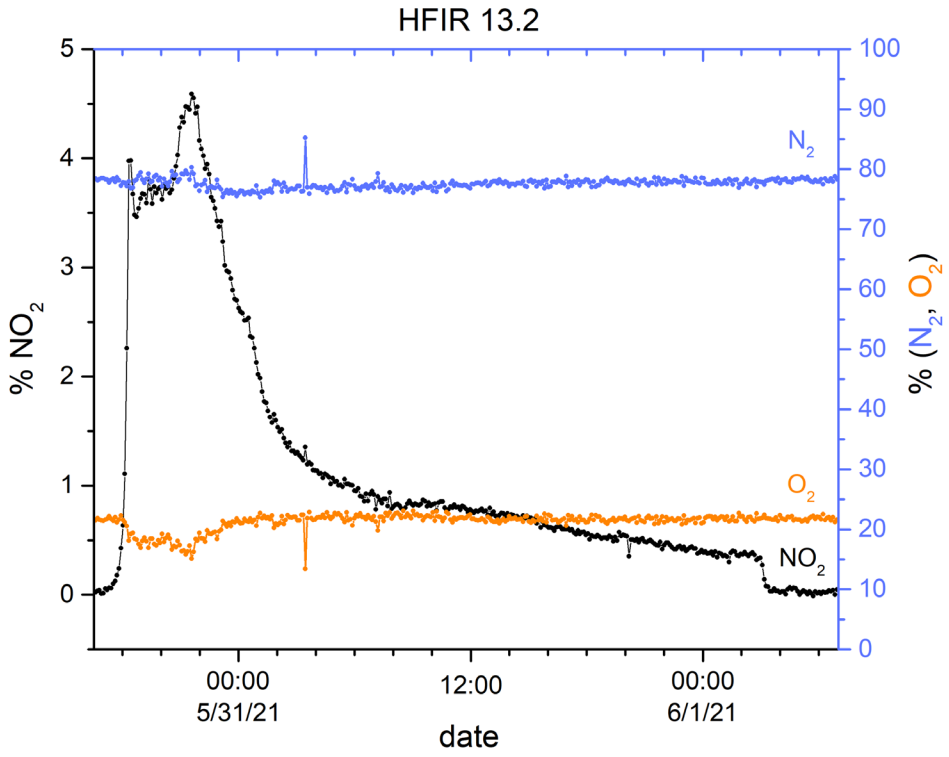

Figure A-14. Offgas evolution, HFIR Batch 13, Charge 2.

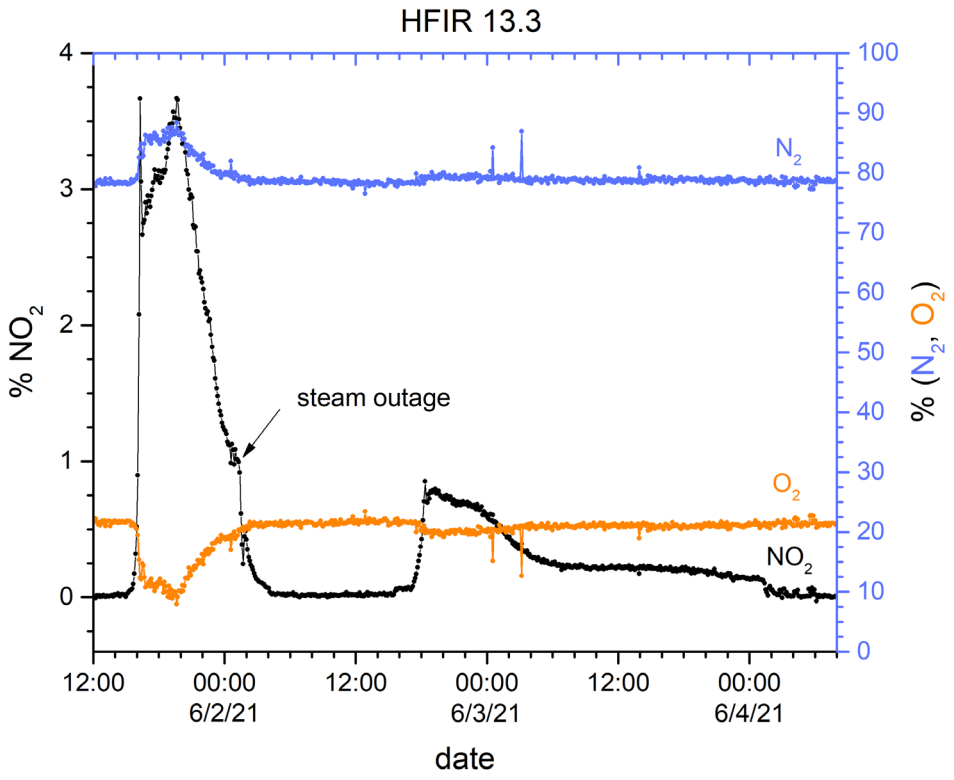

Figure A-15. Offgas evolution, HFIR Batch 13, Charge 3.

Appendix B. Time Evolution of NO_2 Emission – Individual Charges

The following plots show the progress towards 100% of the total NO_2 emissions for 12 of the 15 process runs observed. The process for calculating the integration curves is outlined in the text. Areas of the curves that have been estimated are plotted with thin lines. Note that the runs from MTR Batch 22, Charges 1 and 2 are not shown. For Charge 1, the Raman data is incomplete due an instrument malfunction in the middle of the run. For Charge 2, the $\%NO_2$ levels are substantially depressed, likely due to leaks in the dissolver lid.

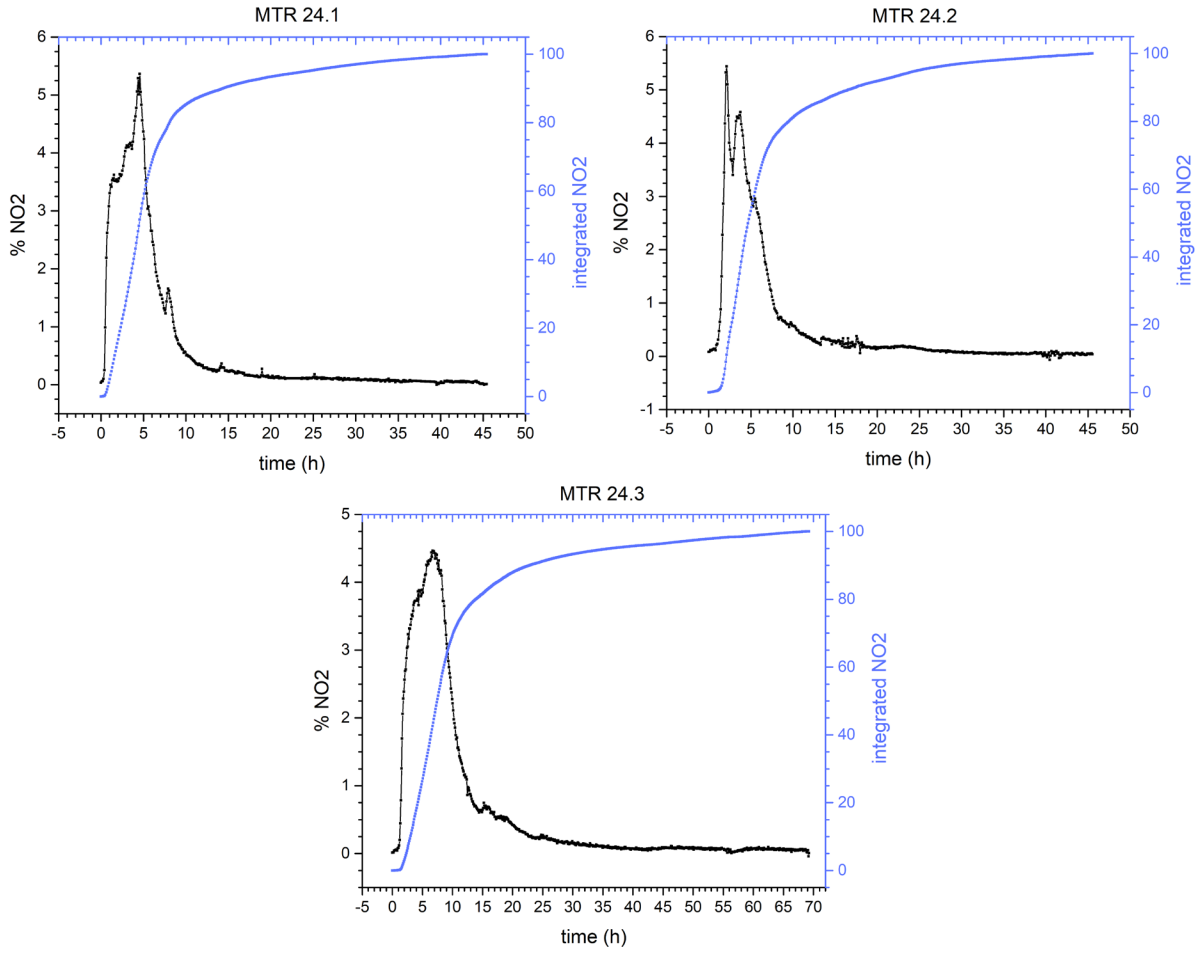

Figure B-1. NO_2 evolution profiles for MTR Batch 24.

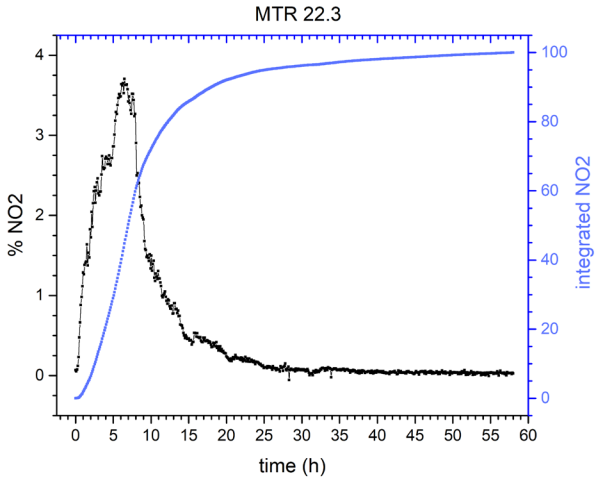

Figure B-2. NO_2 evolution profile for MTR Batch 22.

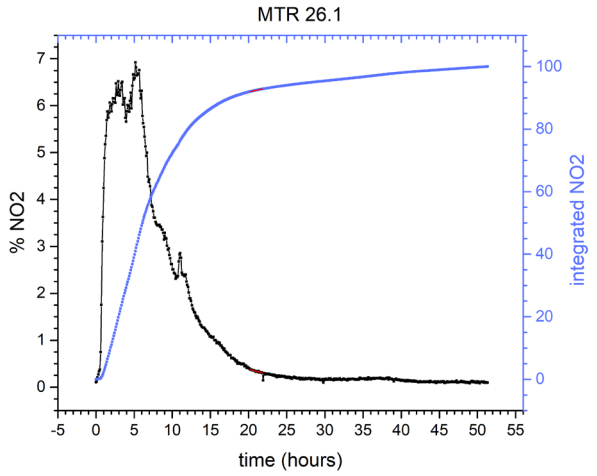

Figure B-3. NO_2 evolution profile for MTR Batch 26.

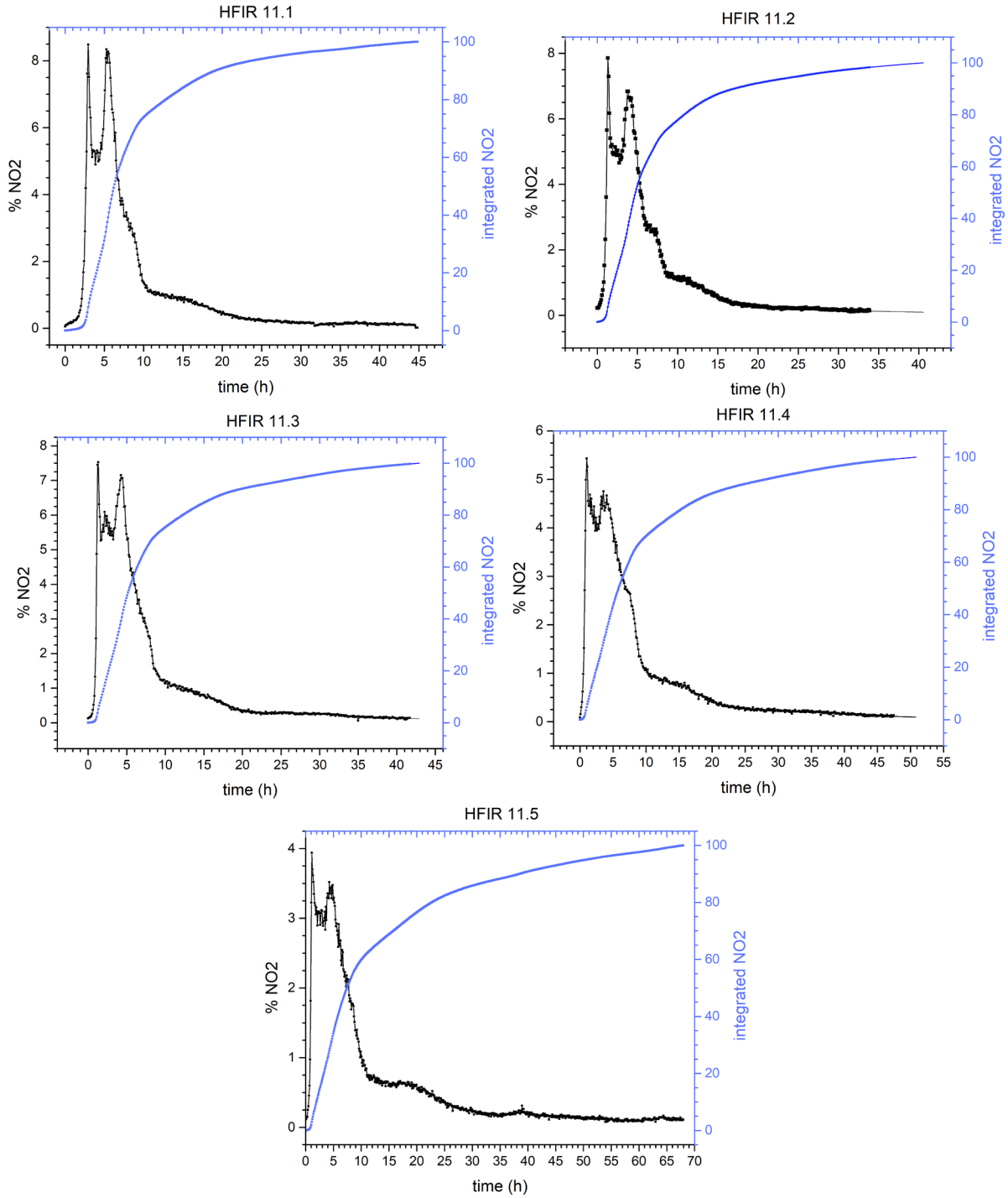

Figure B-4. NO_2 evolution profile for HFIR Batch 11.

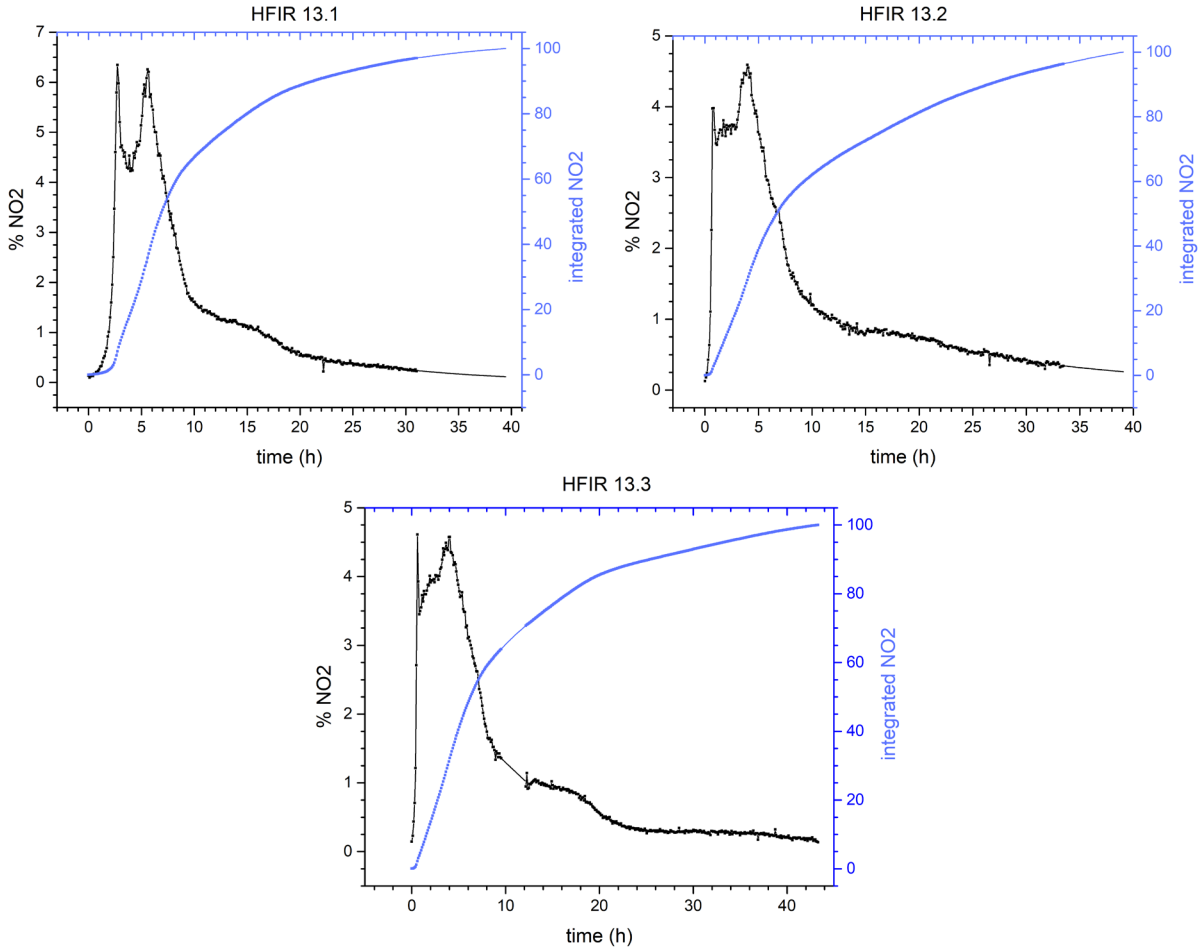

Figure B-5. NO_2 evolution profile for HFIR Batch 13.

Distribution:

H-Canyon:

M.J. Arnold, 221-H
S.J. Brown, 704-2H
K.P. Burrows, 704-2H
W.C. Clark, Jr., 703-H
J.M. Fitzpatrick, 221-H
R. M. Gunby, 221-H
A.M. Hudlow, 704-2H
J.L. Lawson, 703-H
O.L. Rodriquez, 221-H
E. Saldivar, Jr., 703-H
N.A. Smith, 221-H
T.E. Smith, 704-2H
J.E. Therrell, 704-2H

DOE

P.A. Polk, 773-A

SRNL:

C.R. Armstrong, 773-A
M.J. Barnes, 773-A
W.E. Daniel, Jr., 999-W
J.M. Gue, 735-A
D.T. Herman, 735-11A
D.M. Immel, 781-A
R.B. James, 773-A
R.D. Jeffcoat, 735-A
J.M. Mannion, 735-7A
R.L. Minichan, 781-A
P.E. O'Rourke, 999-2W
RA. Pierce, 773-A
M.M. Reigel, 773-A
M.L. Restivo, 773-42A
T.S. Rudisill, 773-A
K.M. Taylor-Pashow, 773-A
T.T. Truong, 773-41A
M.L. Whitehead, 773-A
M.T. Whiteside, 773-A

Other

R.R. Livingston, 730-2B (Omega Technical Services)